Shear wave splitting and waveform complexity for lowermost mantle structures with low-velocity lamellae and transverse isotropy

Melissa M. Moore and Edward J. Garnero

Department of Geological Sciences, Arizona State University, Tempe, Arizona, USA

Thorne Lay and Quentin Williams

Earth Sciences Department, University of California, Santa Cruz, California, USA

[1] Shear waves that traverse the lowermost mantle exhibit polarization anomalies and waveform complexities that indicate the presence of complex velocity structure above the core-mantle boundary. Synthetic seismograms for horizontally and vertically polarized shear waves (*SH* and *SV*, respectively) are computed using the reflectivity method for structures with low-velocity sheets ("lamellae"), and for comb-like models approximating long wavelength vertical transverse isotropy (VTI). Motivated by evidence for partial melt in the deep mantle, lamella parameter ranges include (1) δV_P from -5 to -10%, $\delta V_S = 3\delta V_P$; (2) 100 to 300 km thickness of vertical stacks of lamella; (3) lamella spacing and thickness varying from 0.5 to 20 km; and (4) lamellae concentrated near the top, bottom, or throughout the D″ region at the base of the mantle. Such lamellae represent, in effect, horizontally emplaced dikes within D″. Excessively complex waveforms are produced when more than $\sim 20\%$ of D″ volume is comprised of low-velocity lamellae. Many lamellae models can match observed S_{diff} splitting (1–10 s delays of SV_{diff}), but typically underpredict *ScS* splitting (1–4 s delays of *ScSV*). VTI model parameters are selected to address D″ observations, and include (1) 0.5 to 3% anisotropy; (2) discontinuous D″ shear velocity increases up to 3%; (3) D″ thicknesses from 100 to 300 km; and (4) VTI concentrated at the top, bottom, or throughout D″. VTI models readily match observed splits of *ScS* and S_{diff}. We discuss lamellae and VTI model attributes in relationship to waveform complexities, splitting magnitude, triplications from a high-velocity D″ discontinuity, and apparently reversed polarity SV_{diff} onsets. The possible presence of melt-filled lamellae indicates that local chemical or thermal perturbations can produce regions that exceed the solidus within D″. Such melt could occur in the bulk of D″ because the melt is either close to neutral buoyancy, advective velocities exceed percolative velocities, or both.   *INDEX TERMS:* 7203 Seismology: Body wave propagation; 7207 Seismology: Core and mantle; 7260 Seismology: Theory and modeling; 8124 Tectonophysics: Earth's interior—composition and state (1212); *KEYWORDS:* shear wave splitting, lowermost mantle anisotropy, waveform modeling

1. Introduction

[2] Over the past 20 years, the D″ region in the mantle's lowermost 200–300 km has become a major topic of study in deep Earth research disciplines, including seismology, mineral physics, geodynamics, geochemistry and geomagnetism [e.g., *Loper and Lay*, 1995; *Gurnis et al.*, 1998; *Garnero*, 2000]. D″ is of interest due to its role in the overall dynamics of the Earth; it is the lower thermal boundary layer of the mantle convection system, it controls the heat flux out of the core that affects the geodynamo, and

it overlies the core-mantle boundary (CMB)—the primary internal compositional boundary in the planet. Seismological travel time and waveform studies have provided clear evidence of small- to large-scale heterogeneity in the deep mantle (see reviews by *Lay et al.* [1998a]; *Garnero* [2000]; *Masters et al.* [2000]). Further complexities have been revealed by shear wave polarization studies indicating that D″ has large-scale regions with apparent seismic anisotropy, unlike the bulk of the lower mantle [e.g., *Lay et al.*, 1998b; *Karato*, 1998b; *Kendall*, 2000]. Accurate characterization of any seismic anisotropy or other structure producing complex shear wave polarization in D″ holds great promise for elucidating deep Earth structure and dynamics. In short, the structural origin of D″ anisotropy is critical for assessing

Table 1. Observations of Shear Wave Splitting in D″[a]

Study	Data	$T_{SV} - T_{SH}$, s	Inferred Anisotropy, %	Suggested Anisotropy Geometry
Alaska				
Lay and Young [1990]	S, ScS	0−4	[b]	TI
Lay and Young [1991]	S, ScS	0−4.5	1.5−3	TI
Matzel et al. [1996]	S, S$_{diff}$, ScS	3−5	1.5−3	TI
Garnero and Lay [1997]	S, S$_{diff}$, ScS	0−4	1−1.5	TI
Kendall and Silver [1998]	S, S$_{diff}$, ScS	3−9	1.8	TI
Fouch et al. [2001]	S, S$_{diff}$	0.5−1.5	0.3−0.9	AA/TI
Caribbean				
Mitchell and Helmberger [1973]	ScS	0−3	2	TI
Lay and Helmberger [1983]	ScS	0−4	5	[c]
Kendall and Silver [1996]	S, S$_{diff}$	2−9	0.5−2.8	TI
Ding and Helmberger [1997]	ScS	[b]	2.5	TI
Central Pacific				
Vinnik et al. [1989]	S$_{diff}$	[b]	0.5	AA
Maupin [1994]	S$_{diff}$	[b]	1	AA
Vinnik et al. [1995]	S$_{diff}$	0.5−3	1	TI
Vinnik et al. [1998]	S, S$_{diff}$	−3−9	8−9	TI
Pulliam and Sen [1998]	S	0−2	2−2.5	TI
Ritsema et al. [1998]	S$_{diff}$	0−3	1.4−2.1	TI
Russell et al. [1998, 1999]	ScS	−1−8	2−3	TI
Fouch et al. [2001]	S, S$_{diff}$	0.2−5.7	1.3−5.3	TI
Indian Ocean				
Ritsema [2000]	S	1−3	1.5	TI
Northern Siberia				
Thomas and Kendall [2002]	S, S$_{diff}$, ScS	0−4.8	0.5−1.3	TI

[a]Abbreviations are as follows: TI, transverse isotropy; AA, azimuthal anisotropy.
[b]Not stated.
[c]Suggested that splits are due to velocity structure.

the processes that occur in, and the nature of, this boundary layer. If anisotropy is generated purely by solid-state texturing [e.g., *Karato*, 1998a], then there exist useful analogies with the lithospheric boundary layer. If anisotropy is instead produced by intercalations of partial melt [e.g., *Kendall and Silver*, 1998], then the evolution of this layer might be governed largely by magmatic processes. The purpose of this study is to explore families of models for D″ structure that fall into the latter category, and evaluate how well these models account for observations of deep mantle shear wave splitting and complexity in order to improve our understanding of the structure of the mantle's lower boundary.

1.1. *S* Wave Complexities in D″

[3] Investigations of shear wave polarization in D″ have been conducted beneath several areas, including Alaska, the central Pacific, the Caribbean, Eurasia, and the Indian Ocean (Table 1). The preponderance of the observations involve delays of vertically polarized *S* wave components (*SV*) by up to 10 s relative to horizontally polarized *S* wave components (*SH*) for paths that graze horizontally through the D″ region, as shown in the composite of global observations in Figure 1. Circum-Pacific regions, which tend to have higher than average D″ shear velocities, have 500−1500 km scale regions of relatively uniform splitting behavior of this type, whereas the low-velocity region under the central Pacific has smaller scale regions with *SV* sometimes being advanced by a few seconds relative to *SH* (see reviews by *Lay et al.* [1998b]; *Kendall* [2000]). There is not much evidence for

splitting of *S* waves traveling vertically through D″, such as *SKS* [*Meade et al.*, 1995]. All studies to date are limited by poor azimuthal sampling and uncertainty in upper mantle anisotropy corrections, so characterization of the shear wave splitting is far from complete in all areas. Also, the distinct nature of *SV* and *SH* interactions with the CMB, which results in complex *S* wave polarization at diffracted distances even for simple isotropic structure, complicates quantification of splitting effects within D″ [e.g., *Maupin*, 1994; *Ritsema et al.*, 1998].

[4] Further complicating the situation is the widespread observation of *SH* triplications. These have been attributed to a velocity discontinuity or strong velocity gradient at the top of the D″ layer (see reviews by *Wysession et al.* [1998] and *Lay et al.* [1998a]). While the relationship between shear wave polarization anomalies and the D″ triplication remains unclear, the data suggest that splitting originates within the D″ layer (at and below any discontinuity at the top of D″) [*Lay and Young*, 1991; *Matzel et al.*, 1996; *Kendall and Silver*, 1996; *Garnero and Lay*, 1997]. Indeed, it appears that when present, the D″ discontinuity coincides with a transition from an isotropic to an effectively anisotropic structure [*Matzel et al.*, 1996; *Cormier*, 1999, 2000; *Russell et al.*, 2001]. That the primary discrete geophysical demarcation of the top of D″ is likely generated by the onset of anisotropic texture illustrates the importance of arriving at an improved understanding of the origin of anisotropy in this zone.

[5] In addition to the observations of anisotropy, there is strong evidence for extreme velocity reductions in D″ on scale lengths from tens to hundreds of kilometers [e.g.,
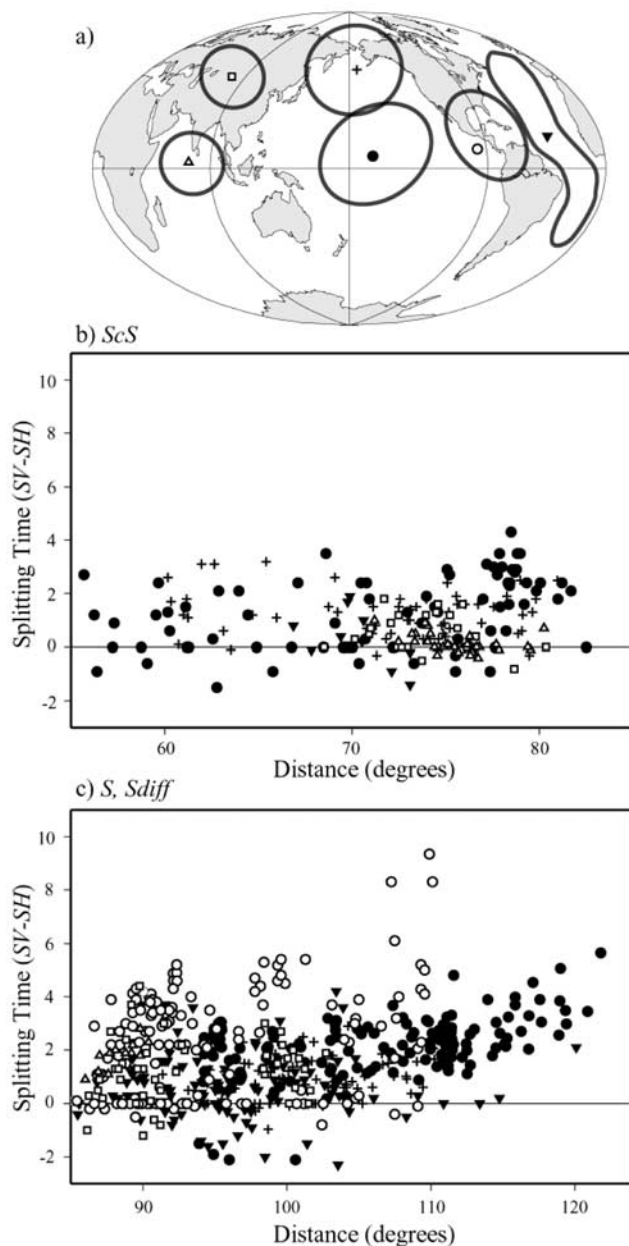
Figure 1. (a) Map of globe indicating locations of shear wave splitting studies. Each regional symbol on the globe corresponds to symbols used in splitting time versus distance plots: (b) compilation of $ScSV–ScSH$ splitting times and (c) compilation of $SV_{diff} − SH_{diff}$ splitting times. Figures 1b and 1c show distance in degrees versus splitting times measured as SV arrival time minus SH arrival time. Splitting times used in Figure 1b include: *Lay and Young* [1991]; *Ritsema* [2000]; *Thomas and Kendall* [2002]; *Garnero and Lay* [2003]. Splitting times used in Figure 1c include: *Lay and Young* [1991]; *Kendall and Silver* [1996]; *Pulliam and Sen* [1998]; *Ritsema* [2000]; *Fouch et al.* [2001]; *Thomas and Kendall* [2002]; *Moore et al.* [2002]; *Garnero and Lay* [2003].

Garnero et al., 1998; *Wen and Helmberger*, 1998; *Garnero*, 2000; *Wen et al.*, 2001; *Wen*, 2002; *Ni et al.*, 2002]. The magnitude of these velocity decrements appear compatible with abundant partial melting within D″, with the amount of melt appearing to be particularly abundant at the absolute base of the mantle [e.g., *Williams and Garnero*, 1996]. Additionally, reflections from isolated thin high- or low-velocity lamella near the top of D″ have also been suggested [*Weber*, 1994; *Thomas et al.*, 1998]. Similarly, the ability of melt-filled inclusions to generate anisotropy within the bulk of D″ has been noted [*Kendall and Silver*, 1996, 1998], but a causal relationship between anisotropy-generating localized melting and possible reflections from lamellae has not been demonstrated. One of our primary goals is to probe the relationship between possible melt-containing lamellae distribution, amplitude and structure, and the genesis of anisotropy within D″.

[6] Such partial melting in D″ is likely to be associated with chemical heterogeneity, and there is now substantial evidence that chemical heterogeneity might exist in D″ based on the more pronounced variations in S velocity relative to those in P velocity [e.g., *Robertson and Woodhouse*, 1996; *Su and Dziewonski*, 1997; *Kennett et al.*, 1998; *Wysession et al.*, 1999; *Masters et al.*, 2000; *Wen et al.*, 2001; *Bolton and Masters*, 2001; *Saltzer et al.*, 2001; *Simmons and Grand*, 2002]. Moreover, the nature of the temperature field within D″ is ill constrained: the canonical one-dimensional view involves a close-to-linear temperature gradient within this thermal boundary layer, with one constant point being the nearly isothermal temperature at the top of the outer core [e.g., *Williams*, 1998]. Yet, lateral variations in temperature certainly exist within D″: depending on the shapes and chemical buoyancies of upwellings and downwellings, the vertical temperature gradients certainly might have large local deviations. The precise interplay between the complex (and dynamic) thermal regime within D″ and the amount and location(s) of melt in a system that is likely near (or above) its solidus remains unclear. Thus, it is quite plausible that chemical heterogeneities, partial melt, thermal variations and their interactions with strong boundary layer shear flows in D″ could affect seismic velocities. These factors, combined with additional causes of shear wave splitting (such as solid-state texturing), must be assessed when shear waveforms such as those in Figure 2 are analyzed. These waveforms sample D″ structure throughout the main regions that have been studied in the past, and thus provide some of our primary constraints on the characteristics of this boundary layer.

1.2. Shear Wave Anisotropy in D″

[7] While complex isotropic structures can explain some attributes of the shear waveform complexity and splitting observations in Figures 1 and 2 [e.g., *Mitchell and Helmberger*, 1973; *Lay and Helmberger*, 1983; *Ritsema et al.*, 1997], there is an emerging consensus that significant regions of D″ are seismically anisotropic (possibly due to chemical heterogeneity, partial melting and strong shear flows), with shear velocity depending on particle motion direction. Typically, for the limited azimuthal sampling available, SH velocities (V_{SH}) a percent or two higher than SV velocities (V_{SV}) match the splitting measurements shown in Figure 1. To first-order, the SH and
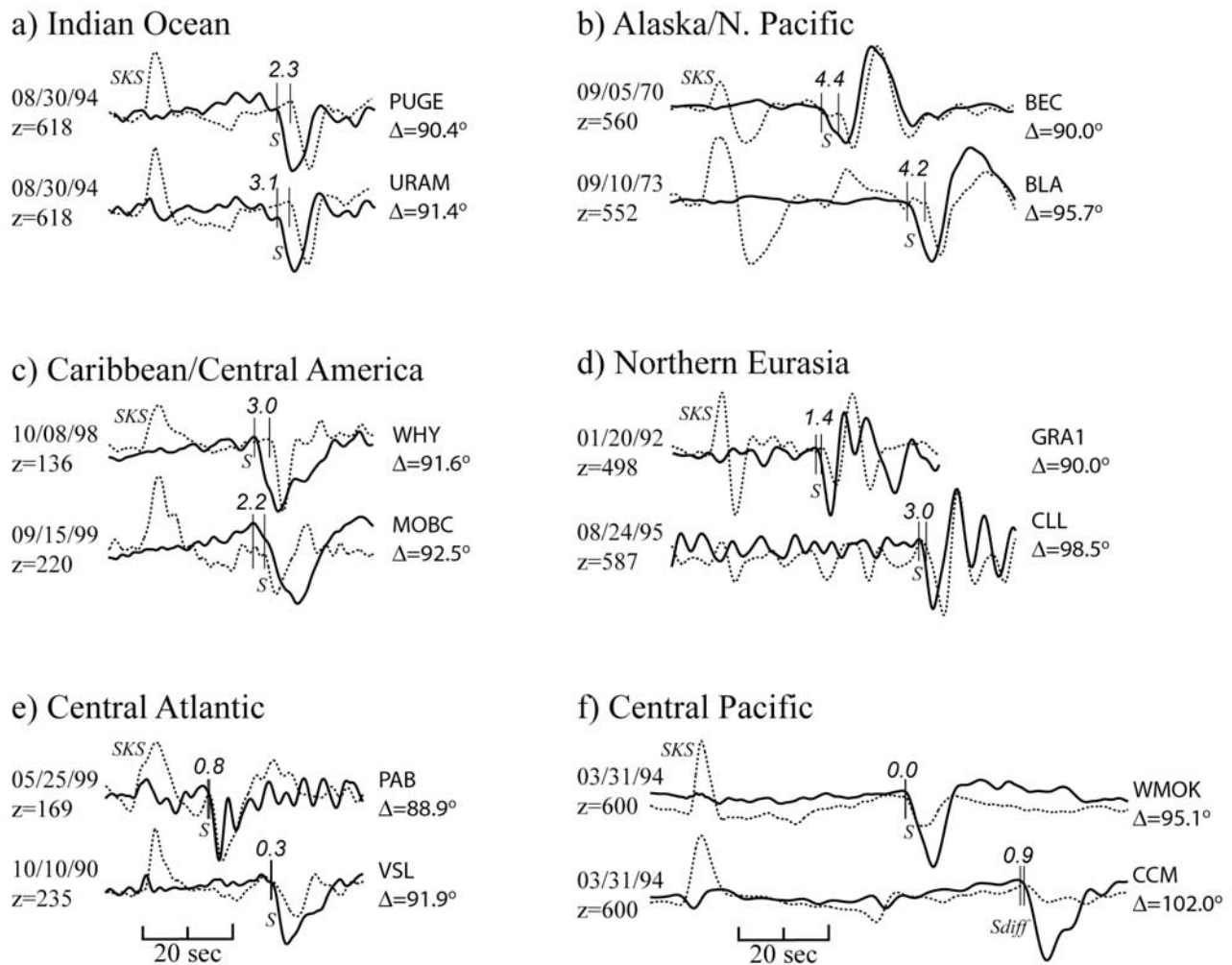
Figure 2. Examples of shear wave splitting measurements in S waveforms. Event date (month/day/year) and depth (z) are indicated to the left, station name and epicentral distance (Δ) to the right of each SV (dashed) and SH (solid) record pair. Splits in seconds are indicated above onsets of S phases. Data are from (a) *Ritsema* [2000], (b) *Garnero and Lay* [1997], (c) *Garnero and Lay* [2003], (d) *Thomas and Kendall* [2002], (e) *Moore et al.* [2002], and (f) *Ritsema et al.* [1998]. Amplitudes are normalized to the maximum amplitude in each trace. Data in Figures 2a, 2c, 2e, and 2f are broadband displacement, in Figure 1b are long period WWSSN, and in Figure 2d are broadband velocity. A variety in splitting strength is present (from 0.0 to 4.4 s).

SV wave fields appear to be decoupled in the D″ layer, meaning that the waveforms in Figure 2 can be accounted for by separate SH and SV velocity models in D″.

[8] On a large scale, the bulk of the lower mantle is thought to be close to seismically isotropic [e.g., *Kaneshima and Silver*, 1995; *Meade et al.*, 1995]. Therefore the onset of anisotropy in the lower boundary layer of the mantle might require distinct conditions from the overlying mantle. One must be cautious in making this inference though, given that conditions for the development of anisotropy in the mid-mantle might intrinsically be highly variable due to temperature, stress and chemical heterogeneity in the convecting mantle system [e.g., *McNamara et al.*, 2001, 2002; *Wookey et al.*, 2002]. Indeed, we view as an open issue the existence and extent of mid-mantle anisotropy, but there is as yet no evidence as clear as that for D″ anisotropy.

[9] There are several possible causes of deep mantle anisotropy involving either the presence of anisotropic crystals in a lattice-preferred orientation (LPO) [e.g., *Stixrude*, 1998; *Karato*, 1998a, 1998B; *McNamara et al.*, 2001, 2002; *Yamazaki and Karato*, 2002] or shape-preferred orientation (SPO) of material with strongly varying seismic velocities [e.g., *Kendall and Silver*, 1996, 1998; *Russell et al.*, 1998; *Wysession et al.*, 1999]. LPO for crystals with a vertical hexagonal symmetry axis (Figure 3a) results in vertical transverse isotropy (VTI), or what is commonly called radial anisotropy. The SH and SV wave fields decouple in this geometry. The mineralogy must be such that horizontally propagating V_{SH} is faster than V_{SV} to be consistent with most of the deep mantle observations. SPO can involve a great variety of geometries, from tubular inclusions to sheets to anastomozing
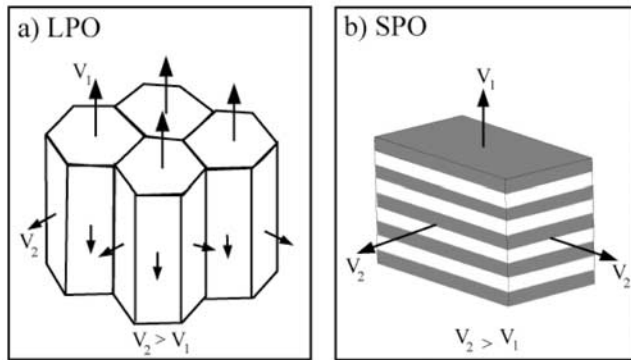
Figure 3. Possible styles of anisotropy in D″ resulting in vertical transverse isotropy (VTI). V_1 represents the shear wave velocity in the vertical direction and V_2 represents the velocity in the horizontal. $V_2 > V_1$, thus VTI. (a) Splitting can be produced by the presence of anisotropic minerals oriented by shear flows to have lattice-preferred orientation (LPO). This requires relatively low temperature, high stress environment dominated by dislocation glide. If the minerals have hexagonal symmetry with a vertically aligned symmetry axis, the result will be VTI. (b) Thin alternating sheets (lamellae) of strongly contrasting elastic properties parallel to the CMB (hence, shape-preferred orientation, SPO). These thin alternating layers (gray and white) have strongly contrasting velocities, with very low velocities in the partially melted layers. If there is favorable statistical distribution of the layering, the medium approaches VTI.

structures. Strong shear flows in the boundary layer could align chemical and/or partially molten heterogeneities into vertical or horizontal fabrics. The class of SPO involving horizontally sheared sheets of material might be approximated by one or more thin lamella with strong material property contrasts relative to the matrix, and we explore such models in this paper. If shearing results in horizontal sheets of melt or chemical heterogeneities (Figure 3b), the effect should be to produce interference effects with $V_{SH} >$ V_{SV}. SPO with other geometries must be explored by effective medium theory [e.g., *Kendall and Silver*, 1998] or by scattering approximations [e.g., *Cormier*, 2000], until three-dimensional numerical modeling becomes viable. VTI with V_{SH} higher than V_{SV} can be approximated by periodic thin isotropic layers with strongly contrasting properties (Figure 3a), as long as appropriate scaling is present for the seismic wavelengths of interest [*Backus*, 1962]. We exploit this latter fact to examine a continuum of models ranging from limited numbers of low-velocity lamellae which produce S waveform and polarization complications but not effective anisotropy, to periodically layered lamella models originating from either SPO or LPO, which approximate VTI with $V_{SH} > V_{SV}$.

[10] In this study, we explore radial distributions of lamellae structures and VTI in D″. Features such as a D″ velocity discontinuity and thin ultra-low-velocity layers are incorporated as we consider suites of models that might hold in different parts of D″. In essence, a portion of our modeling is designed to explore the viability and possible role of dike- or sill-like structures in explaining the seismic properties of D″: the ubiquity of diking in magmatic

systems in both the lithosphere and asthenosphere is well documented, and we would view it as surprising if some formation of dike-like features did not occur in association with a partially molten layer at the base of the Earth's mantle. Our goal is thus to assess structures that produce the magnitude of observed S, S_{diff}, and ScS splitting (e.g., Table 1 and Figure 1), constrained by overall waveform characteristics (e.g., Figure 2). A main result of this paper is that important waveform and travel time consequences arise for certain model features and types, allowing us to place bounds on viable structures. Complete waveform considerations are shown to be important, since predicted D″ anisotropy can be in gross error when inferred from splitting times and D″ path lengths derived from 1-D ray tracing for an isotropic D″ reference velocity structure. While unique interpretations of shear wave complexity are not yet viable, various possibilities can be ruled out, and necessary conditions can be established for the types and distribution of dike-like structures in this region of the planet.

2. Synthetic Seismogram Modeling

[11] Synthetic seismograms are generated for one-dimensional radial velocity profiles using the reflectivity method (for layered isotropic media) [*Fuchs and Müller*, 1971; *Kind and Müller*, 1975; *Müller*, 1985]. SH and SV waveforms are computed for the distance range 65°–120°, enabling analysis of S and ScS at shorter distances (<80°) and S and S_{diff} at larger ranges (>90°). Periods of ~5 s and longer are computed, as this corresponds to the periods of the primary observations. We consider two classes of models: suites of isolated low-velocity lamellae and laminated (periodic) structures yielding effective VTI. This can be viewed as a continuum of lamellae models, although the VTI endmember can also be viewed as a parameterized form of LPO anisotropy (for a radial hexagonal symmetry axis with $V_{SH} > V_{SV}$ in the horizontal plane). While one-dimensional (1-D) models are clearly of limited applicability to the heterogeneous D″ region, data do display regional coherence over relatively large-length scales, particularly in circum-Pacific regions, so we view our modeling as characterizing regional scales. Numerical modeling of 2-D and 3-D heterogeneous and anisotropic structure might eventually be viable, but observational constraints on such models will continue to be very limited for some time to come.

2.1. Lamellae Models

[12] Individual thin layers with very strong velocity contrasts (increases or decreases) in D″ have been proposed based on waveform observations [e.g., *Mitchell and Helmberger*, 1973; *Lay and Helmberger*, 1983; *Weber*, 1994; *Thomas et al.*, 1998], with the best evidence being for a thin low-velocity layer right at the CMB [e.g., see *Garnero et al.*, 1998]. The notion of more complex, multiple lamella has been raised by *Kendall and Silver* [1996, 1998], who used effective medium theory modeling with high- and low-velocity inclusions that were disk- or cigar-shaped. The latter geometries were found to be less effective in generating SPO and not suitable to explain most D″ observations. It was found that very low aspect ratio (0.001) disk-shaped melt inclusions with inclusion volume fractions of <0.0001 can create 2% anisotropy, and *Kendall*

Table 2. Synthetic Model Parameters

Parameter	Values Tested
Lamellae Model Synthetics	
Lamellae thickness, km	0.5, 1, 5, 10, 15, 20
Spacing between lamellae, km	0.5, 1, 5, 10, 15, 20
Overall thickness of lamellae stack, km	100, 200, 300
V_P to V_S ratio in lamellae	1:3
% V_P: V_S reductions[a]	5:10; 10:30
VTI Model Synthetics	
Thickness of D″, km	100–300
Thickness of TI zone, km	25, 50, 75, 100,150, 200, 250, 300
SH D″ discontinuity velocity increases,[a] %	0, 2, 4, 6, 8
Anisotropy strength,[b] % †	0, 1, 2, 3, 4, 5

[a]Relative to PREM.
[b]V_{SV} reduction relative to *SH*.

and Silver [1998] noted that their calculations are very similar to those for a periodic thin-layered medium. They concluded that either partial melting within a horizontally sheared former oceanic crustal layer or folding over of a low-velocity crustal layer could produce SPO in D″ compatible with observations under the Caribbean, but synthetics were not produced and the scale lengths of the implied structures were not examined. Moreover, the association of these possible melt-containing disks with subducted crustal material remains speculative: while we do not preclude this possibility, there are a broad range of additional processes that could generate partial melting within the D″ region. These include, but are not limited to, eutectic melting of a pyrolitic mantle [*Williams and Garnero*, 1996; *Holland and Ahrens*, 1997; *Zerr et al.*, 1998], melting due to contamination by core-derived material, and melting produced by viscous heating [*Steinbach and Yuen*, 1999].

[13] Given that the relevant *S* wave data have 5–10 s predominant periods, there are intrinsic bounds on lamellae distributions and scale lengths imposed by the waveform behavior. We seek to quantify those bounds by considering a wide range of lamellae models for which we make synthetic seismograms (see Table 2). Clearly, we cannot hope to resolve the smallest scales that are viable, which might extend to melt films on individual crystal grains (as explored by effective medium theory). However, we can assess the vertical extent of D″ material which has any macroscopic lamination.

[14] Initial calculations were made for individual or small numbers of lamella with varying properties. These models give rise to reflections and internal reverberations that have distinct characteristics for *SH* and *SV* wave fields, but do not match observed *ScS* or S_{diff} splitting and can account for only limited aspects of waveform complexity such as triplication arrivals, so we do not consider those models further in this paper. Rather, we consider models with constant, positive, or negative gradients of low-velocity lamellae over substantial zones of D″ (Figure 4, "L" equals lamella thickness). Over 350 profiles of *SH* and *SV* synthetics were generated. We restricted our modeling to low-velocity lamellae with partial melt characteristics (δV_P: $\delta V_S = 1:3$) [*Williams and Garnero*, 1996], given that there are no obvious candidate D″ materials with large velocity increases, as noted by *Kendall and Silver* [1998]. *Wysession*

et al. [1999] note that reconciling *P* and *S* velocities in D″ can further constrain the anisotropy, but there are relatively poor constraints on *P* velocity in most areas with clear *S* wave splitting, so we focus on the better characterized *S* wave behavior.

[15] Our synthetics demonstrate that when less than ∼15–20% of the volume of D″ is comprised of low-velocity thin lamellae (e.g., <5 km thick with relatively large interlayer spacing, up to ∼10 times the lamella thickness) shear wave splitting is produced that matches the range of observed splitting times. Increasing the volume percent of lamellae in D″ results in synthetics too complex to measure splitting. This is demonstrated by Figure 5, which shows synthetics at 70 and 100 degrees epicentral distances for a 200 km thick D″ layer with uniform equally spaced lamella. *SH* (thick lines) and *SV* (thin lines) synthetics are shown for *ScS* in panel (5a) and S_{diff} in panel (5b). Synthetics for the PREM reference model [*Dziewonski and Anderson*, 1981] are the top pair of traces in each panel, and show the expected coincidence of the *ScS*
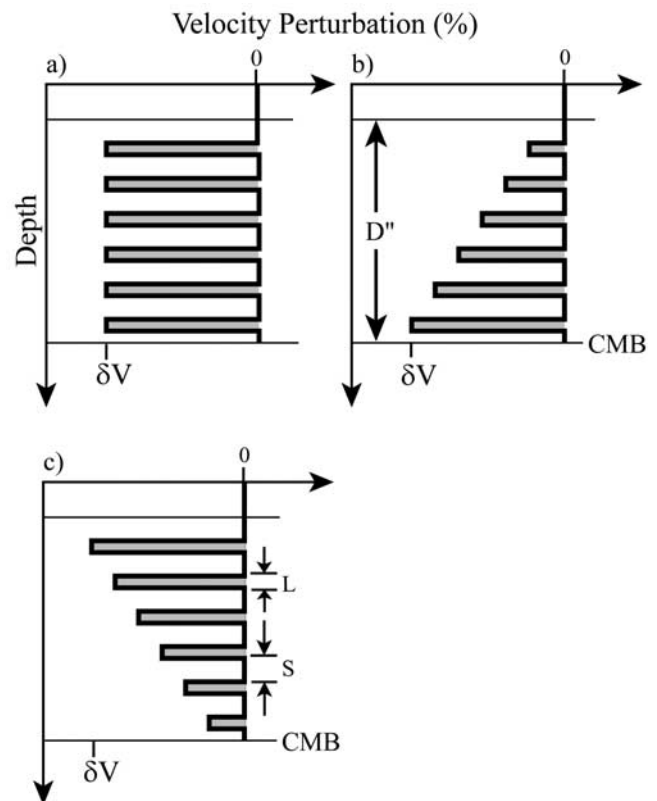

Figure 4. Lamellae model distributions explored in this study: (a) lamellae distributed evenly over D″ thickness of 50, 100, 200, or 300 km. (b) with anomalies concentrated at the bottom of D″ with lamella distributed with a linear gradient from 0% δV at the top of D″ to maximum δV at the CMB, and (c) with anomalies concentrated at the top of D″ with lamella distributed with a linear gradient from 0% δV at the CMB to maximum δV at the top of D″. Lamella thickness (L) and interlayer spacing (S) ranged from 0.5 km to 20 km. Lamella δV_S: δV_P ratio is 3:1, representing partial melting. Velocity deviations relative to PREM of −5 to −10% for V_P and −15 to −30% for V_S were used.
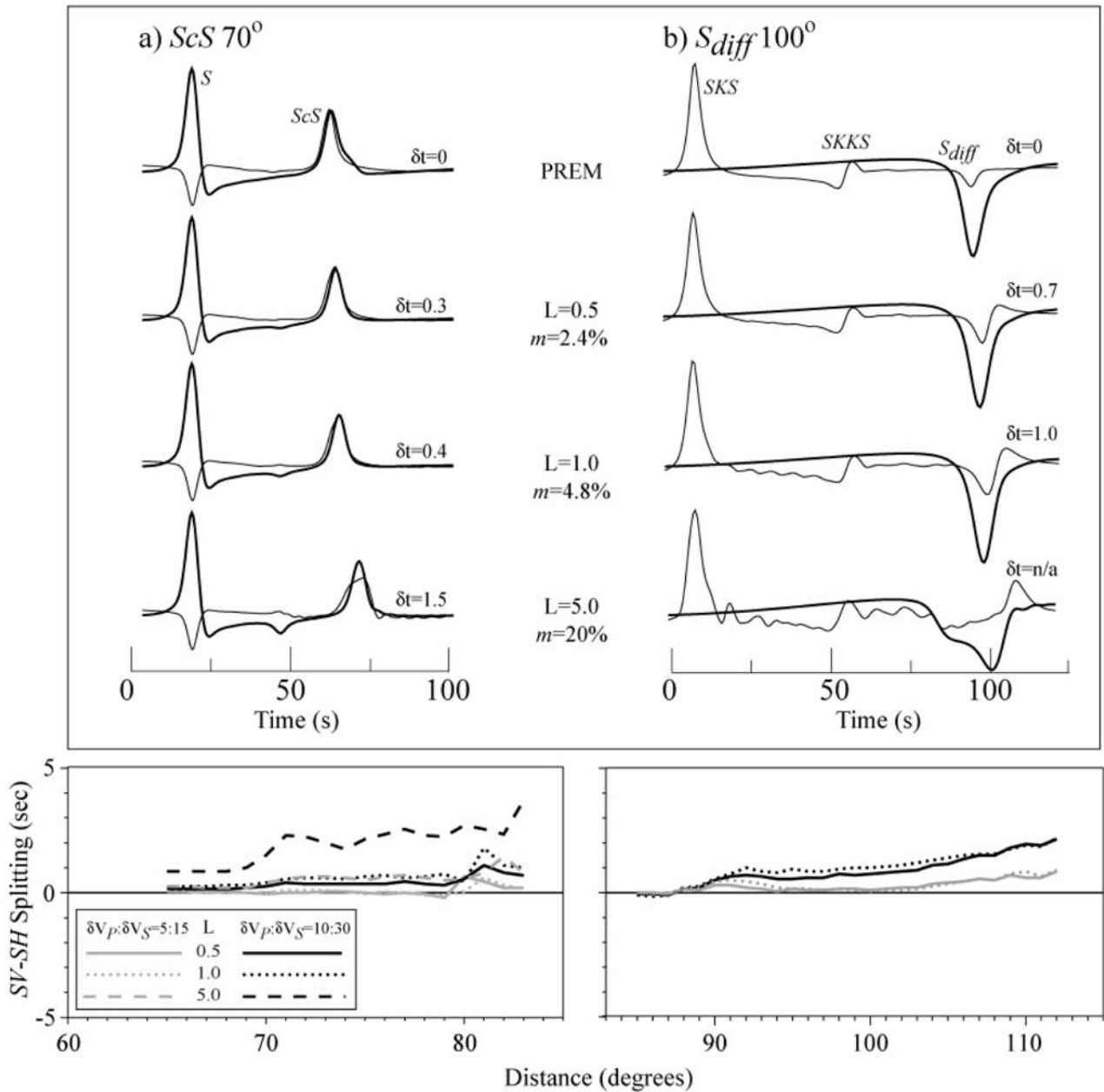
Figure 5. Effects of lamella thickness on synthetic waveforms for distances of 70° and 100°. Synthetics for a 200 km thick D″ layer with lamellae properties of $\delta V_P = -10\%$ and $\delta V_S = -30\%$ are shown. Interlamella spacing is 20 km and lamella thickness (L) varies from 0.5 km to 5 km. SH seismograms are heavier lines, while SV seismograms are lighter lines. Differential times of the SV and SH first arrivals (δt) are shown to the right of each trace pair when the first arrival is clear. The percent of D″ that occupied by lamellae (m) is also indicated on the figure. Synthetics for PREM [*Dziewonski and Anderson*, 1981] at the specified distance are shown at the top of each column. (a) S and ScS synthetics at 70°. Amplitudes are normalized to $S(SH)$. (b) SKS, $SKKS$, and S_{diff} synthetics at 100°. Amplitudes are normalized to SKS. The travel time plots show SV–SH splitting (seconds) versus distance (degrees). Thickness of lamellae is indicated in the figure legend (L), and given in km. Stronger lamellae reductions ($\delta V_P = -10\%$, $\delta V_S = -30\%$) are shown in black. Gray lines represent times measured from synthetics generated with weaker lamellae properties ($\delta V_P = -5\%$, $\delta V_S = -15\%$). The L = 5.0 km waveforms (for $\delta V_P:\delta V_S = 10:30\%$) were too complex to measure splitting for the S_{diff} range.

and S arrivals on the SV and SH components of motion. The next three pairs of traces in Figures 5a and 5b correspond to lamellae models with δV_P and δV_S reductions of -10% and -30%, respectively, lamella thicknesses (L) of 0.5, 1.0, or 5.0 km, and interlayer-lamella spacing of 20 km. For example, the L = 0.5 traces below the PREM synthetics in Figure 5 are for a repeating pattern of 0.5 km thick low-velocity lamella and 20 km of ambient mantle—hence this model is composed of 10 low-velocity layers (the last mantle layer thickness may vary to result in a 200 km thickness of the overall stack of lamellae). In what follows, we refer to the percent of melt volume in D″ for such models, defined by the percent of the overall thickness of the D″ layer cake occupied by the lamellae. This is indicated in Figure 5 by an italicized m ("melt"): as the ultra-low-velocity zone (ULVZ) decrements of velocity are used for these molten zone, the actual melt contents within these lamellae is 6–30% of the values of the italicized m, and depend on the geometric distribution of the partial melt [*Williams and Garnero*, 1996]. Because of this geometric uncertainty in melt abundance, we simply report the net volumes of the partially molten lamellae, rather than their associated (and uncertain) melt fraction. Our rationale for using the velocity decrements of the ULVZ is that melt has apparently been unable to segregate from its coexisting solid within the ULVZ itself, and we anticipate that any upwellings derived from the ULVZ are likely to be composed of a similar liquid-solid aggregate.

[16] For periods of $\sim 5-10$ sec, complex SV waveform behavior occurs for lamella thickness greater than a few km, as in the bottom pair of traces in Figure 5b. The first arriving SKS phase is followed by ringing of energy, due to multiple reverberations within and between individual lamella, particularly for stronger velocity perturbations. Clear data (with good signal-to-noise ratios) do not show these waveform complexities. For ScS synthetics, waveforms for thick lamellae layering are less affected than for S_{diff}.

[17] For the thin lamella with 20 km interlayer spacing, the net waveform effect is a smooth interference that distorts the SV waveform relative to SH, yielding an apparent S wave onset splitting of up to a few seconds, along with some overall S-SKS differential time increase. Shear wave splitting versus distance is also presented in Figure 5. A general trend of increasing splits with distance is shown, which falls within the general range of observations (Figure 1). Stronger velocity reductions cause larger splitting magnitudes. Synthetic results for 5 km thick lamella are not shown in the 85–115 degree distance range because the waveforms are too complex to be characterized by a simple shift of the onset times. All shear wave splitting measurements in this paper were measured both by hand (SH and SV onset times for S waves and peak times for ScS), and also by waveform cross-correlation of the SV and SH components of ScS or S observations with those of PREM predictions. Most data measurements (Figure 1) have been based on hand picking. In our synthetics the interfering arrivals generated by lamellae sometimes obscure the onset of the SH and SV pulses, making onset time picks uncertain. Even for the PREM synthetics the SV waveform differs from SH (for core grazing and diffracting S waves), primarily due to destructive interference with $ScSV$ in contrast

to constructive interference with $ScSH$, with associated differences in diffraction effects for the two components. A challenge for waveform cross correlation measurements is that S and S_{diff} waveshapes depart significantly from PREM for the more anomalous lamellae models (e.g., Figure 5b, L = 5 km). While there is uncertainty associated with both splitting measurement methods, cross-correlation gave more consistent measurements for our synthetics, and is used throughout this paper.

[18] While Figure 5 demonstrates that excessively thick lamellae eventually produce some waveform distortions, it is important to point out that the ratio between lamellae thickness and spacing, S/L, and thus the D″ volume % melt, is the fundamental factor that relates to an effective anisotropy. This permits no limit to how thin lamellae can be (and hence the number of lamellae occupying D″).

[19] In Figure 6, we fix L at 1 km with δV_P and δV_P reductions equaling -10% and -30%, respectively, and vary interlamella spacing. The material between lamella, i.e., from the top of one lamella to the bottom of the overlying lamella, varies from 5 to 20 km in thickness and has the properties of PREM. For the 1 km thick lamella, interlamella spacing greater than 10 km is required to produce smooth interference patterns that can match the observed waveforms. Smaller spacing between lamellae involves a significant percentage of D″ being occupied by melt-rich lamellae ($\sim 15\%$ volume and greater), which results in trapped energy that creates additional arrivals not observed in data, at least for the stronger velocity anomalies. Thus we see that the higher melt volume percentages result in anomalously broadened any multi-valued SH_{diff} and SH_{diff}. These effects are particularly acute for thicker lamella (Figure 6, bottom) where splitting times cannot be assessed at the larger distances.

[20] Interlamella spacing thickness does depend on minimum lamella thickness: thinner spacing can be accommodated if lamellae are thinner. Synthetics for models with 5 km lamella thickness and 20 km spacing have similar overall waveforms to those for models with 1 km lamella and 5 km spacing. Therefore it is the percentage of D″ comprised of lamellae that is the important factor in the resulting waveform. All models with the same volume of melt give comparable splitting except (1) when the spacing is too large compared to the wavelength of the seismic wave and internal multiples give rise to waveform distortions and/or (2) when individual lamella are too thick and begin trapping significant energy, thus resulting in waveform distortions. Also note that the percentage of D″ occupied by "melt" lamellae, i.e., low-velocity structure, cannot be in a contiguous zone. Rather they must be in thin sheets (subwavelength scales) that are spaced relative to one another to produce shear wave splitting. Less than 10% partial melt volume is typically required to obtain synthetic waveforms compatible with observations.

[21] Differential times for models with 1 or 5 km thick lamellae are shown in Figure 6 below the seismograms. In general, models with more than 15–20% of D″ occupied by low-velocity lamellae result in excessively complex waveforms with interference effects that are not characterized by simple shear wave splitting. Shear wave splitting times are not measurable for many records with extreme waveform complexities, leading to omission of some model results in
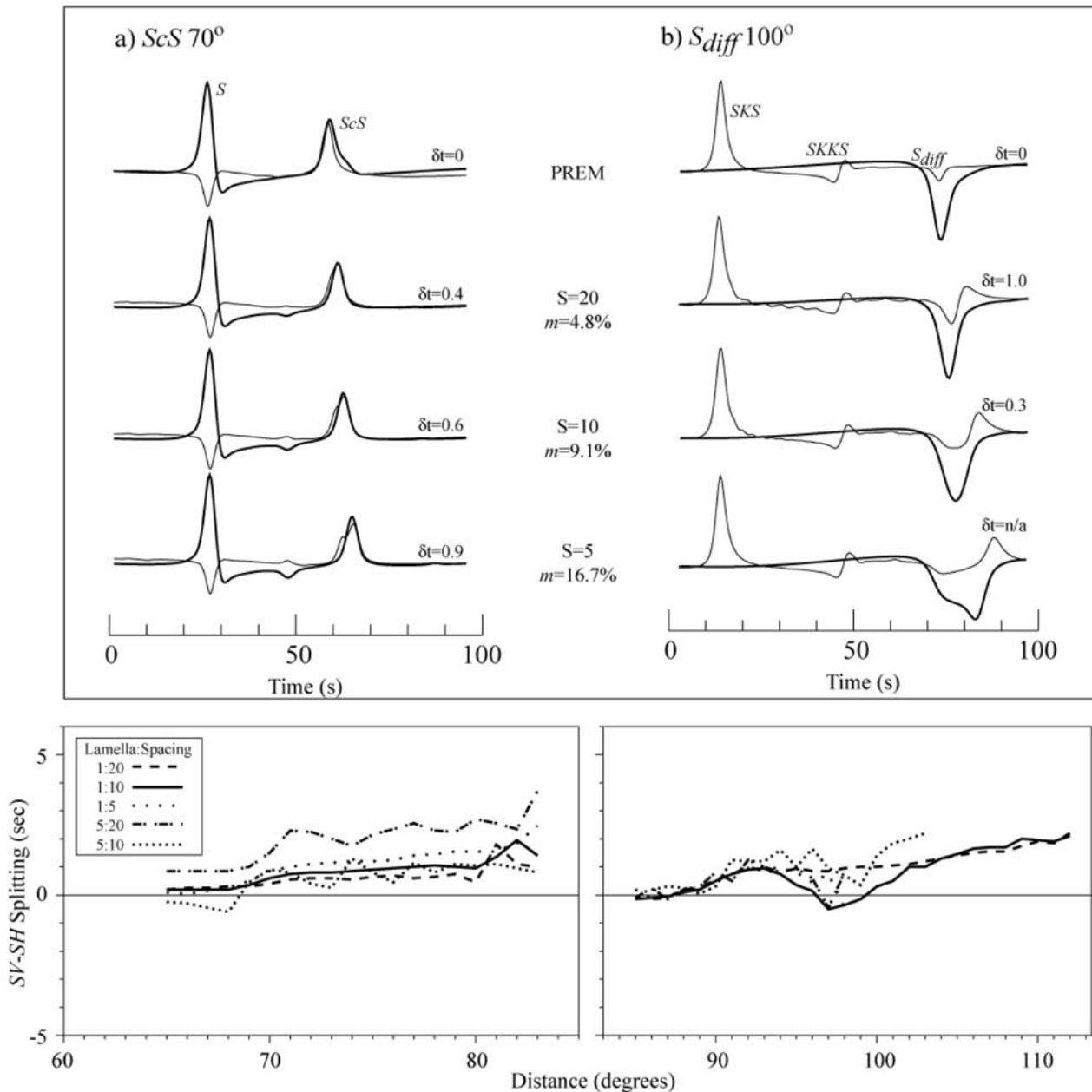
Figure 6. Effects of interlamella spacing (S) on synthetic waveforms at 70° and 100° degrees, for uniform lamella thickness of 1 km throughout a 200 km thick D″ zone. S is varied from 20 to 5 km. S and m (D″ lamellae volume fraction) are indicated between the columns of synthetics. (a) S and ScS waveforms at 70°. (b) SKS, SKKS, and S_{diff} waveforms at 100°. Travel time plots show $\delta V_P{:}\delta V_S$ reductions of 10:30% for lamellae distributed throughout D″ (as in Figure 4a) for various thicknesses of lamella and lamella spacing. Curves that do not span the entire distance range represent models from which waveforms were too complex to measure splitting. All other conventions are as in Figure 5.

the travel time panels (or results being shown over a limited distance range.)

[22] The calculations in Figures 5 and 6 indicate that models with lamella thickness equaling the interlayer spacing are not acceptable due to excessive waveform complexity (at least in the model space of discrete lamellae with partial melting). The upper bound of ~15% on lamellae concentration is compatible with the notion that partial

melting or low-velocity heterogeneities comprise a minor component of the lowermost mantle.

[23] The depth extent over which lamellae are distributed in D″ also affects the waveforms. In Figure 7 the thickness of the lamellae zone varies from 100 to 300 km. All other model parameters are kept constant (1 km thick lamellae, 20 km spacing, $\delta V_P = -10\%$, $\delta V_S = -30\%$: for reference, assuming these zones are associated with 6–30% partial
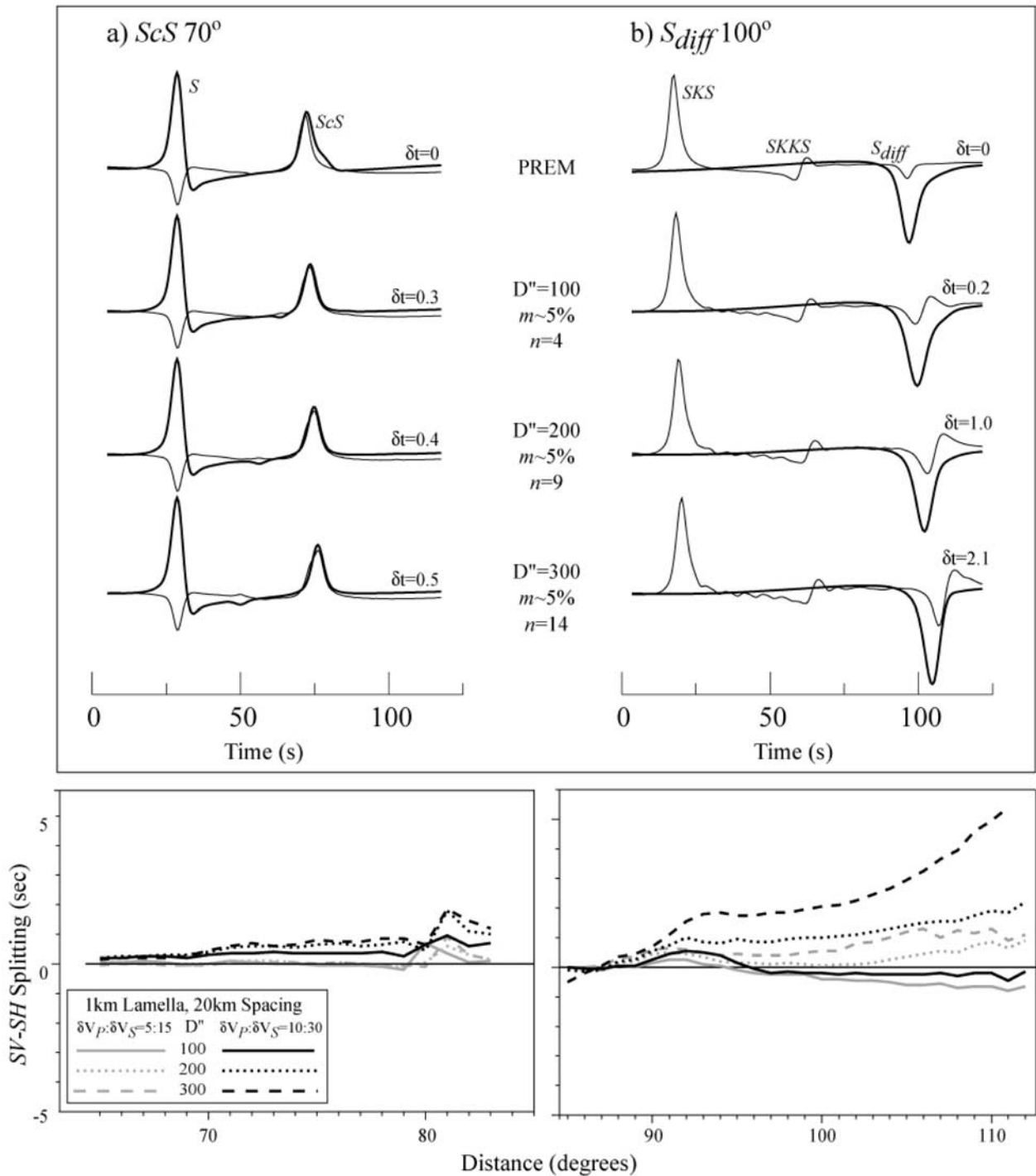
Figure 7. Model tests of variable thickness of D″ lamellae zone. (See Figures 5 and 6 for figure conventions.) Synthetics contain 1 km thick lamella, 20 km interlamella spacing, with lamellae properties of δV_P, $\delta V_S = -10\%$, -30% throughout a D″ thickness of 100, 200, or 300 km. D″ thickness (D″) in km, percent of D″ occupied by lamellae (m), and the number of lamella layers within D″ (n) are shown between the columns of synthetics. (a) S and ScS waveforms at 70°. (b) SKS, SKKS, and S_{diff} waveforms at 100°. Travel time curves show $SV-SH$ splitting times (seconds) versus distance (degrees). δV_P, $\delta V_S = -10\%$, -30% are indicated by black lines and δV_P, $\delta V_S = -5\%$, -15% are shown in gray.

melt [*Williams and Garnero*, 1996], we derive a rather small $\sim 0.3-1.5\%$ melt fraction in D″). A thicker lamellae stack produces slightly more complex waveforms than PREM (e.g., see Figure 7b, in which the 300 km thick D″ displays

low amplitude ringing), but each D″ thickness produces stable and clear ScS and S_{diff} waveforms that are comparable to observations. Increasing the thickness of the lamellae stack produces progressively larger shear wave splitting,
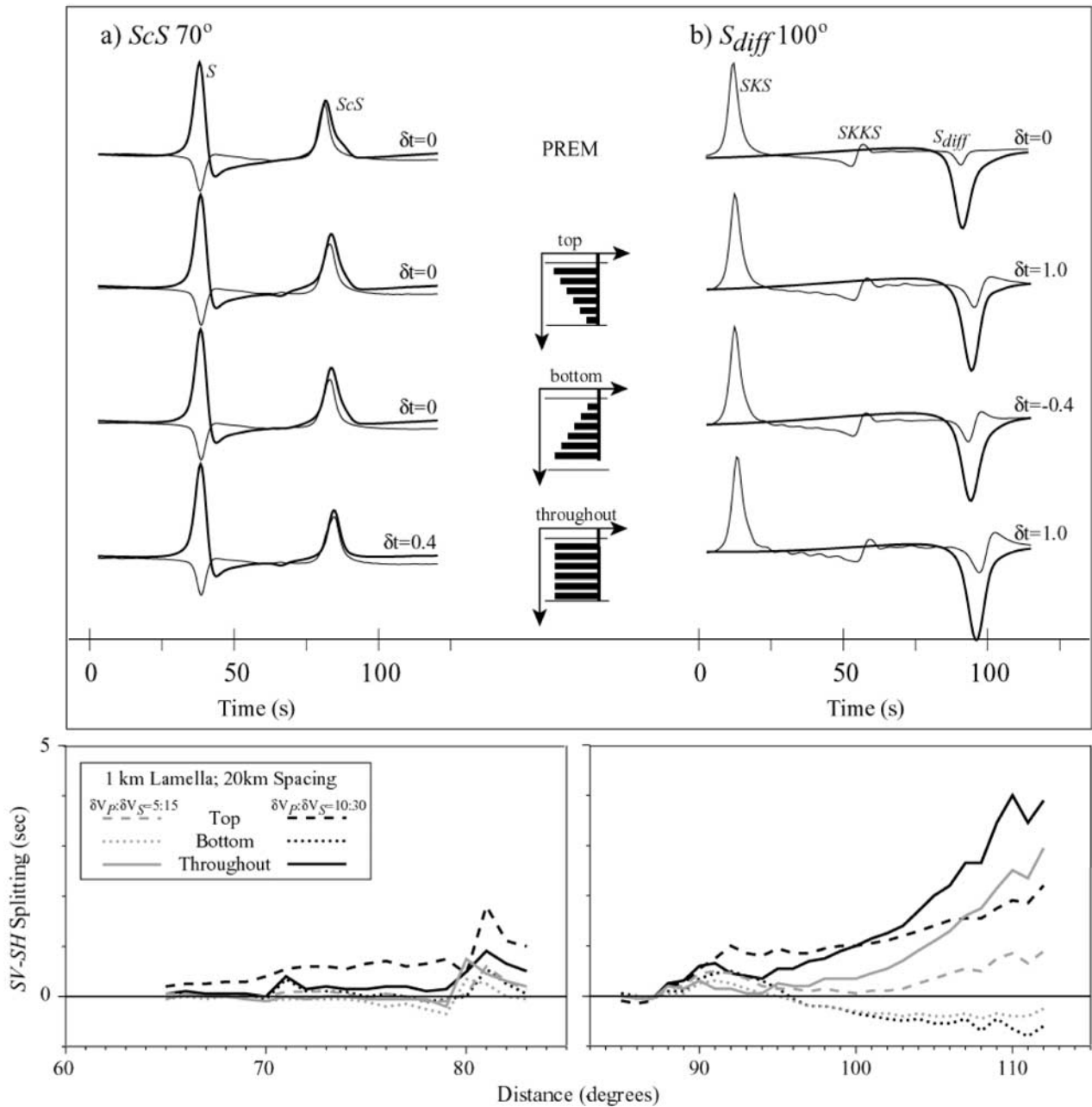
Figure 8. Synthetics for varying D″ lamellae distributions over a thickness of 200 km, with 1 km thick lamellae and 20 km spacing. Synthetics for (a) S and ScS, and (b) SKS, SKKS, and S_{diff} are shown for PREM and lamellae with $\delta V_P = -10\%$ and $\delta V_S -30\%$. (See Figure 5 for other details.) SV–SH splitting times versus distance is shown in bottom panels.

along with a modest increase in S–SKS differential time. For a 100 km thick stack of lamellae, there is virtually no splitting, while a 300 km thickness yields splitting of 2.1 s for an S wave at a range of 100°. These models contain 5 to 15 low-velocity layers in the boundary layer, which would require strongly folded and sheared heterogeneities.

[24] We also explored the effects of concentrating lamellae toward the top or bottom of D″ (Figure 8). Synthetics are constructed for models containing lamellae stacks 200 km thick, with 1 km lamella thickness and 20 km interlayer spacing. The strength of the velocity anomalies in the

lamellae is tapered upward or downward from the peak anomalies either at the top of the 200 km lamellae zone or at the CMB (as indicated in the Figure 8). The S_{diff} range (Figure 8b) displays shear wave spitting for the differing depth-dependent lamellae distributions. When lamellae are concentrated near the top of D″, the strongest splitting occurs, owing to the larger time spent in the strongest lamellae layers for core grazing and diffracted wave fields, as compared to concentrating lamellae at the bottom of D″. A counterintuitive result is that for the case of uniform lamellae throughout D″ the splitting is less than for lamellae
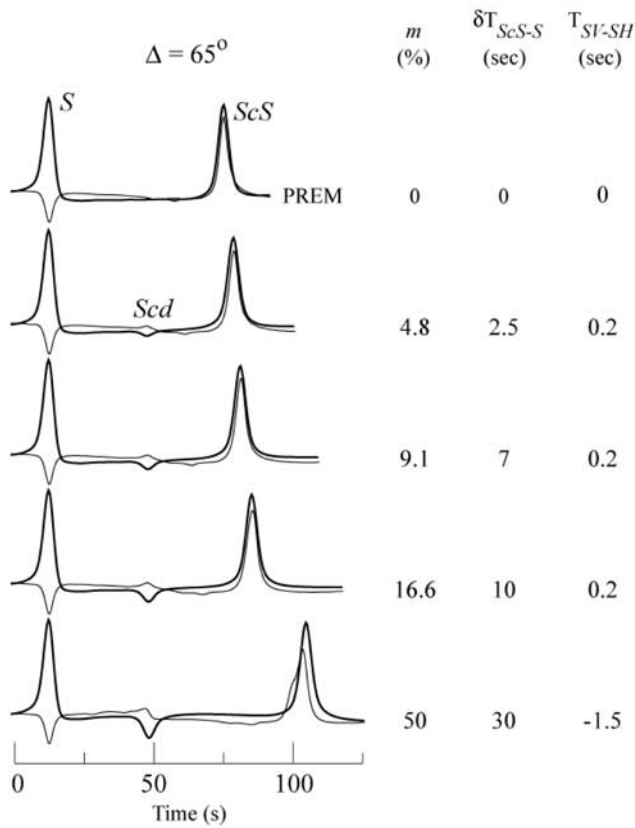
Figure 9. Sensitivity of *ScS* travel times to lamellae models. Synthetics for *S* and *ScS* are shown for distances of 65° for PREM and lamellae models of varying interlayer spacing with 1 km thick lamellae uniformly distributed over a 300 km thick D″ layer with −10% and −30% reductions of V_P and V_S, respectively. *SH* seismograms are heavier lines, while *SV* seismograms are lighter lines, and the traces are aligned on *S*. Amplitudes are normalized to *S*. The percent of D″ occupied by lamellae (*m*), delay times of ScS relative to the PREM synthetics (δT_{ScS-S}, model - PREM), and *SV*–*SH* splitting time (T_{SV-SH}) are shown to the right of each synthetic pair.

concentrated at the top of D″. This is due to significant *SV* energy being trapped in the strongest low-velocity lamellae at the top of D″, while SH energy can propagate in the less anomalous structure toward the base of D″. Thus, pervasive

diking or sill-formation near the top of D″ is particularly effective at generating shear-wave anisotropy.

[25] In Figures 7 and 8, the ∼5% D″ lamellae volume (1 km lamella, 20 km spacing between lamella) results in only mild splitting (≤1 s) for most of the *ScS* distance range. This falls short of the strongest observed *ScS* splitting (up to ∼3–4 s, Figure 1a). At *ScS* distances, primarily <80°, the *ScS* wave traverses the lamellae models more steeply than S_{diff}, resulting in relatively less splitting. One characteristic of the *ScS* waveforms computed for lamellae models is a differential travel time anomaly between *ScS* and *S*. Figure 9 shows *ScS* synthetics at 65° for a 300 km thick D″ containing uniform lamella with $\delta V_P = -10\%$ and $\delta V_S = -30\%$ with examples for different interlamella spacing. Here we write δT_{ScS-S} to denote the *ScS*–*S* travel time anomaly relative to the prediction of the PREM reference structure, measured as $[ScS–S]_{\mathrm{Model}} − [ScS–S]_{\mathrm{PREM}}$. These values are listed to the right of the synthetic seismogram in Figure 9. Note the lack of splitting of the *ScS* arrivals for this distance. As the volume of lamellae occupying D″ increases, the strength of reflections from the top of the stack (*Scd*) grows and the *ScS* phase is increasingly delayed. The *Scd* reflections have opposite polarity to those previously noted in the literature [e.g., see *Wysession et al.*, 1998] due to the negative velocity discontinuity at the top of the first lamella. It is interesting to note how little complexity arises from layers of low-velocity lamella due to the interference between reflections.

[26] While we do not find significant splitting for *ScS* phases for the lamellae models, there is a clear distance dependence of onset shifts for *S* phases. To better understand the different features of the vast models space, we show Figure 10 as a summary figure of some of the characteristics seen in the synthetics. The first five examples focus on lamellae that are distributed throughout D″. In Figure 10a, a 200 km D″ with 0.5 km lamella and 20 km spacing is shown. Lamellae properties have values of $\delta V_P = -5\%$, $\delta V_S = -15\%$, hence a ∼2.4% melt fraction in D″ (nine lamellae). At shorter distances, around 90° to 100°, the waveshapes remain fairly stable with only small to moderate splits. As epicentral distance increases (∼105°–115°) an offset of the phase onsets begins to be seen but a reduction of SV_{diff} amplitude precludes measuring the *SV*–*SH* times. Figure 10b shows a 200 km thick D″ containing 1 km lamella and 20 km spacing (4.8% melt volume) with an increase in inferred melt strength:

Figure 10. Summary figure for different classes of lamellae models. Seismograms are shown in distance (degrees) versus relative time in seconds. All traces are aligned in time on the S_{diff} and amplitudes are scaled to the largest amplitude in the time window. *SKS*, *SKKS*, and S_{diff} arrivals are indicated. *SH* is indicated by the dashed lines and *SV* by the solid lines. A schematic of each model is shown above each set of seismograms. (a) 200 km D″ with 0.5 km lamellae and 20 km spacing. Lamella properties are $\delta V_P = -5\%$ and $\delta V_S = -15\%$ throughout D″. (b) 200 km D″ with 1 km lamellae and 20 km spacing. Lamella properties are $\delta V_P = -10\%$ and $\delta V_S = -30\%$ throughout D″. (c) 200 km D″ with 5 km lamellae and 20 km spacing. Lamella properties are $\delta V_P = -10\%$ and $\delta V_S = -30\%$ throughout D″. (d) 200 km D″ with 5 km lamellae and 20 km spacing. Lamella properties are $\delta V_P = -5\%$ and $\delta V_S = -15\%$ throughout D″. (e) 300 km D″ with 1 km lamellae and 20 km spacing. Lamella properties are $\delta V_P = -10\%$ and $\delta V_S = -30\%$ throughout D″. (f) 200 km D″ with 1 km lamellae and 20 km spacing. Lamella properties are $\delta V_P = -10\%$ and $\delta V_S = -30\%$ at the top of D″ with a gradient down to 0% velocity anomaly at the CMB. (g) 200 km D″ with 1 km lamellae and 20 km spacing. Lamella properties are $\delta V_P = -5\%$ and $\delta V_S = -15\%$ at the top of D″ with a gradient down to 0% velocity anomaly at the CMB. (h) 200 km D″ with 1 km lamellae and 20 km spacing. Lamella properties are $\delta V = 0\%$ at the top of D″ with a gradient down to $\delta V_P = -10\%$ and $\delta V_S = -30\%$ at the CMB. Additional phases are also present, such as at 114°: *SPdKS* immediately follows *SKS*, and a precursor to *SKS*, *SpKS*, due to the impedance contrast at the top of the lowermost lamella. See text for further details.
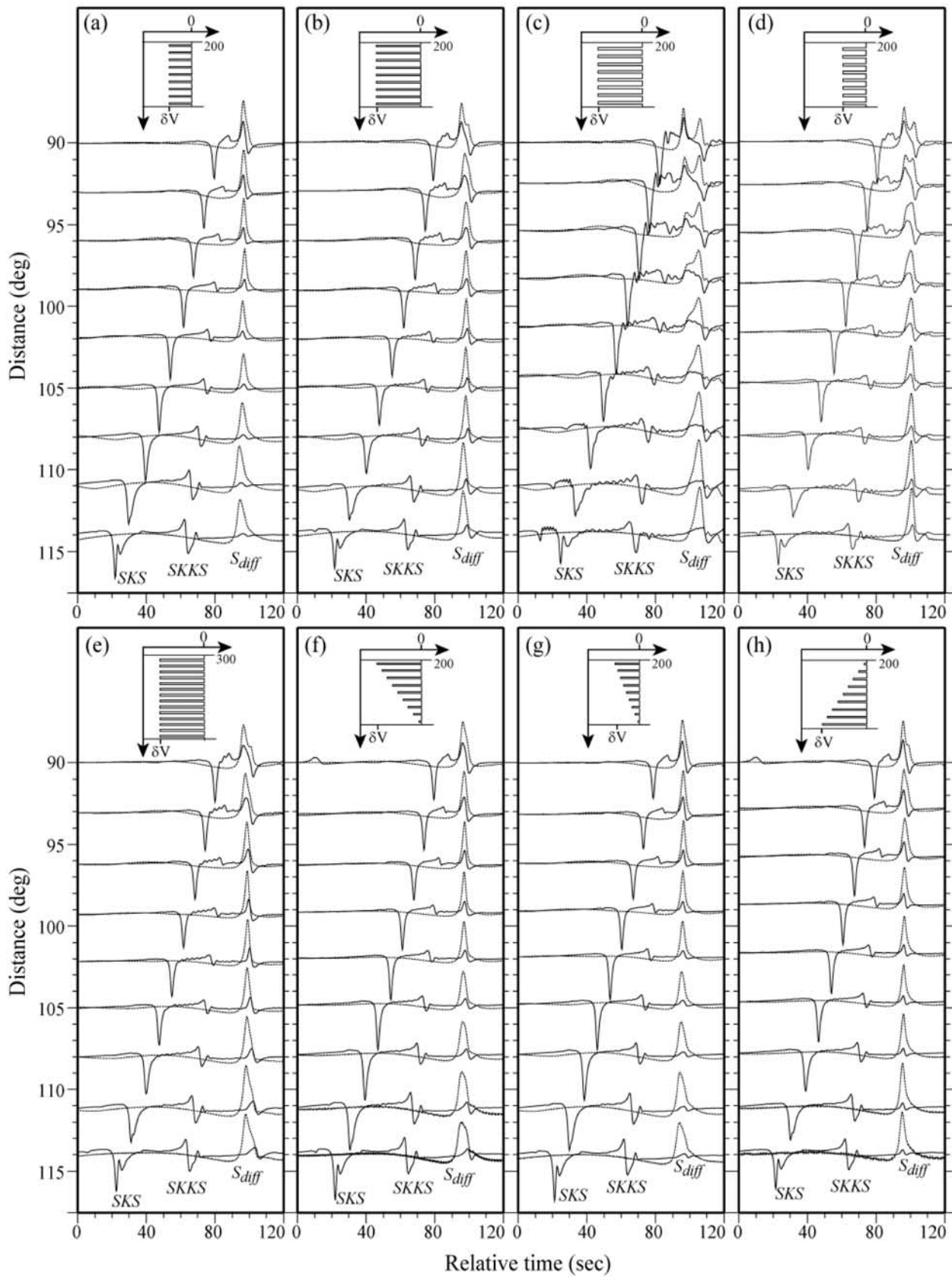
Figure 10.

$\delta V_P = -10\%$, $\delta V_S = -30\%$. Here we see sharpening of SV_{diff} phase onsets at larger distances, with amplitudes sustained more adequately than in Figure 10a. Note that in both Figures 10a and 10b that periodic low-velocity lamellae have the ability to create shear wave splitting. In Figure 10c, melt volume is increased with 5 km lamella and 20 km spacing (200 km thick D″). Melt has properties of $\delta V_P = -10\%$, $\delta V_S = -30\%$. At 20% melt volume in D″ and increased lamella thickness of 5 km we begin to see substantial ringing from energy trapped between in and between the layers (four layers). This increase in melt volume, as well as increased strength in melt properties, might play a role in the ringing noise that develops in the waveforms as we move from Figures 10a to 10b. Figure 10d shows the effect of decreasing the strength of the melt properties from $\delta V_P = -10\%$, $\delta V_S = -30\%$ to $\delta V_P = -5\%$, $\delta V_S = -15\%$. Here the same parameters as Figure 10c are kept except melt strength is decreased. This reduction of δV_P and δV_S lowers the amplitude of the ringing as well as less anomalous SV and SH waveforms. Figure 10e shows results for D″ thickness of 300 km, with 1 km lamella and 10 km spacing, resulting in substantially more layers (27). This thicker D″ and increase in lamella results in bigger splits that have good waveform shapes at larger epicentral distances. However, at core-grazing distances the synthetics are complex. Figures 10f and 10g illustrate characteristics of models that have lamella concentrated at the top of D″. Figure 10f shows a 200 km D″ with 1 km lamella and 20 km spacing. δV_P and δV_S have values of −10% and −30%, respectively, diminishing to 0% at the CMB. There is a substantial amount of energy traveling in the low-velocity lamellae at the top of D″ causing large splits which are not measurable at the larger distances due to SH complexities. If melt properties are decreased, as in panel (g), to $\delta V_P = -5\%$, $\delta V_S = -15\%$ at the top of D″, splitting and SH complexity are reduced, but a large decay in SV amplitude occurs after 105°. In comparison to Figure 10f, Figure 10h contains the same properties except lamella is concentrated at the bottom of D″. Because wave energy is spending less time trapped in the lamella at the bottom of D″, less anomalous wave characteristics are seen than in Figure 10f.

[27] Figure 11 directly compares lamellae models of various D″ melt volumes. The models are computed for a 250 km thick lamellae stack. For this D″ thickness and weaker properties of $\delta V_P = -5\%$, $\delta V_S = -15\%$, 2.5–15% melt volume yields splitting values comparable to data, up to ∼2 s. For models with stronger properties of $\delta V_P = -10\%$, $\delta V_S = -30\%$, only $m = 2.5$–10% reproduces observed times. For melt volumes greater than 10%, the waveforms become increasingly complex and splitting becomes difficult to quantify. These modest numbers of low-velocity lamellae in D″, with properties compatible with partial melt, can thus account for the waveforms and apparent splitting observed in broadband S wave data at distances greater than 90°. However, because these models only begin to simulate effective anisotropy at grazing angles, they do not simultaneously match the ScS observations of Figure 1. Matching these observations requires a more extensive lamination that simulates an overall effective anisotropy of the medium over a broader range of incidence angles for the wave-
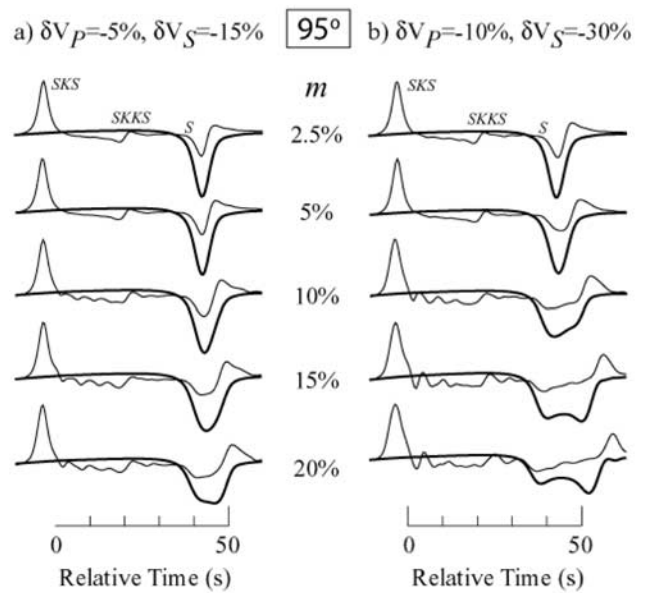

Figure 11. Resultant waveforms of varying D″ lamellae (melt) volume, m. In these models, D″ thickness is set at 250 km, and the waveforms shown are at 95°. SH seismograms are heavier lines, while SV seismograms are lighter lines, and the traces are aligned on SKS. Amplitudes are normalized to SKS. Varying D″ melt volume for lamella with properties of (a) $\delta V_P = -5\%$ and $\delta V_S = -15\%$ and (b) $\delta V_P = -10\%$ and $\delta V_S = -30\%$.

lengths considered. We consider such models in the next section.

2.2. Vertical Transverse Isotropy Models

[28] The second class of models that we explore approximates long wavelength VTI using periodic layering following the medium averaging rules of *Backus* [1962]. This involves alternating strong material property fluctuations from layer to layer that are constrained to achieve a desired fabric anisotropy rather than to conform to expected relationships for an effect such as partial melting. Thus we explore isotropic parameters that effectively approximate anisotropic properties of the medium. Using a one-dimensional reflectivity method for models with horizontal layering limits us to consideration of VTI with $V_{SH} > V_{SV}$, so we cannot address the modeling of any observations displaying SV arriving before SH (hence, implying $V_{SV} > V_{SH}$).

[29] We use thin (1 km) alternating layers with contrasting properties to approximate VTI, according to the *Backus* [1962] formulation. Several examples of VTI models and the alternating isotropic layers that approximate them are given in Table 3. The required V_P and V_S values to achieve VTI vary, and can contain contrasts in the alternating layers as high as 23% for V_P and 33% for V_S. The parameter value η controls the variation of velocities with the angle of propagation [*Backus*, 1962; *Pulliam and Sen*, 1998]. We chose $\eta = 0.95$ for all VTI calculations, following *Pulliam and Sen* [1998], who were able to obtain a good match to S–SKS data.

[30] We consider models with uniform VTI over various portions of D″ for a range of D″ discontinuity strengths and

Table 3. Example Properties of Long Wavelength VTI From Alternating Layers

Model		Desired VTI Velocity Parameters					Equivalent Alternating Velocities, km/s Isotropic Layer			
D″ SH discontinuity, %	VTI, %	V_P^{horiz}, km/s	V_P^{vert}, km/s	V_S^{horiz}, km/s	V_S^{vert}, km/s	η	$V_P^{layer\,A}$	$V_P^{layer\,B}$	$V_S^{layer\,A}$	$V_S^{layer\,B}$
0	2	13.62	13.62	7.24	7.10	0.95	12.13	14.98	6.48	7.93
0	4	13.62	13.62	7.24	6.95	0.95	14.53	12.54	6.15	8.20
2	2	13.62	13.62	7.39	7.24	0.95	12.41	14.70	6.61	8.09
4	2	13.62	13.62	7.53	7.38	0.95	12.66	14.47	6.74	8.25

strengths of anisotropy. Synthetics were calculated for VTI zones throughout D″ thicknesses of 100, 200 or 300 km (e.g., see Table 2). Additional calculations were made for a D″ thickness of 250 km, an approximate average discontinuity height above the CMB obtained from past waveform modeling studies [see *Wysession et al.*, 1998], with the variable thickness of the zone of VTI at the top of D″ measuring 25, 50, 75, 100, and 150 km. VTI strengths that were tested include 2, 4, 6, and 8%. We first address models having VTI from the CMB up to a designated depth (see Figure 12). These models either involve VTI spanning all of D″ (Figures 12a and 12b) or some fraction of D″ from the CMB upward (Figures 12c and 12d), and include models either having or lacking a discontinuity at the top of the VTI zone (see also Table 2). We consider models where the discontinuity coincides with the onset of VTI. Discontinuity strengths that were tested include −2, −1, 0, 1, 2, and 3%.

[31] Figure 13 displays example ScS and S_{diff} waveform and splitting behavior for the model types of Figure 12. For the ScS wave field, fairly stable waveforms and moderate splitting is achieved. ScS splitting shows clear dependence on the thickness of the anisotropy zone—the 300 km thick anisotropic D″ yields the strongest splitting for both ScS and S_{diff}, as expected. When the upper boundary of D″ contains a first order discontinuous increase in velocity, a reflection between S and ScS, the Scd arrival, is apparent in the waveforms (Figure 13c). Thicker D″ layers result in the Scd arrival moving further in front of ScS. The effect of the fast layer is also seen in the 100 degree synthetics, where the SH traces display a characteristic double pulse; the first of the two is Scd, energy propagating in D″, the second is Sab, energy traveling just above the discontinuity [see *Lay and Helmberger*, 1983]. In Figures 13b and 13c, the SV component of S_{diff} (hereinafter, SV_{diff}) is simple in shape and delayed relative to SH. When D″ contains a V_{SV} reduction relative to the overlying mantle, the amplitude of SV_{diff} is increased (as discussed by *Vinnik et al.* [1989]; *Maupin* [1994]). This is seen by comparing the relative SV_{diff}/SKS amplitude ratio in Figure 13b to that of Figure 13c. The suite of models shown in Figure 13 produces shear wave splittings that match the range of observed times (see travel time curves at bottom of Figure 13 and compare to observed times of Figure 1).

[32] A variety of models were explored that contain a zone of VTI at the top of D″ underlain by isotropic velocities down to the CMB. Figure 14 schematically shows example structures containing a VTI layer that initiates at the top of D″. For these structures, the isotropic velocity below the VTI zone is the same as the SH velocity in the VTI zone. Synthetics for a 250 km thick D″ layer with a VTI zone embedded in the top 75 km of D″ are shown in

Figure 15. ScS and S_{diff} synthetics are presented for variable discontinuous SH increases at the top of D″ (from 0 to 3%), holding the strength of VTI fixed at 2%. Increasing the SH discontinuity increases the SHcd amplitude, with the SVcd amplitude being weaker due to the anisotropy reducing the discontinuity for SV. Only minor ScS splitting is predicted by these models due to the limited vertical extent of the VTI zone (Figure 15a). At larger distances (e.g., 100 degrees, Figure 15b) for the same suite of models, the S_{diff} waveforms vary strongly with the strength of the SH discontinuity, and splitting is significant. SV_{diff} waveform complexities, however, make the splitting measurement difficult for the models containing a discontinuity with magnitude 2% or more, primarily due to the relatively high SV velocities down to the CMB. As the thickness of the VTI zone grows from 75 to 125 km, the waveform effects on SV become even more pronounced, with significant effects on the energy turning below the discontinuity.
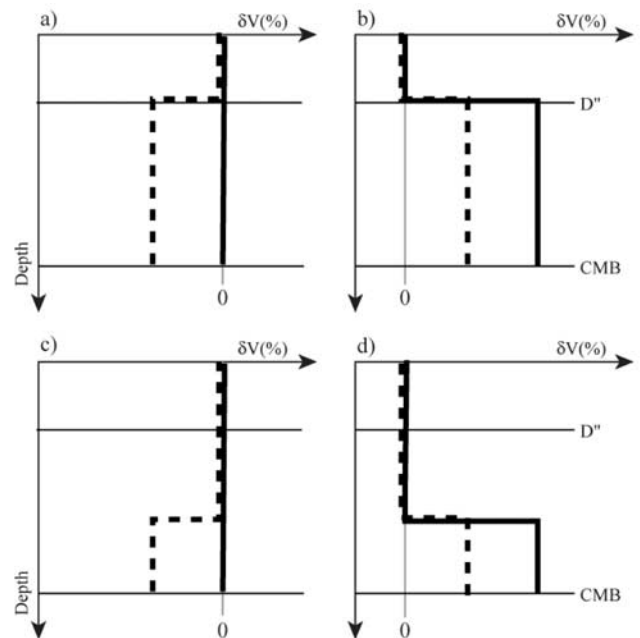

Figure 12. VTI distributions in D″ relative to PREM (vertical zero line). Schematics show percent δV with depth. Solid and dashed lines represent the profiles of V_{SH} and V_{SV}, respectively. (a) VTI zone distributed throughout D″ with no V_{SH} discontinuity. (b) VTI zone distributed throughout D″ with a V_{SH} discontinuity. (c) VTI zone at the bottom of D″ with no V_{SH} discontinuity. (d) VTI zone at the bottom of D″ with a V_{SH} discontinuity.
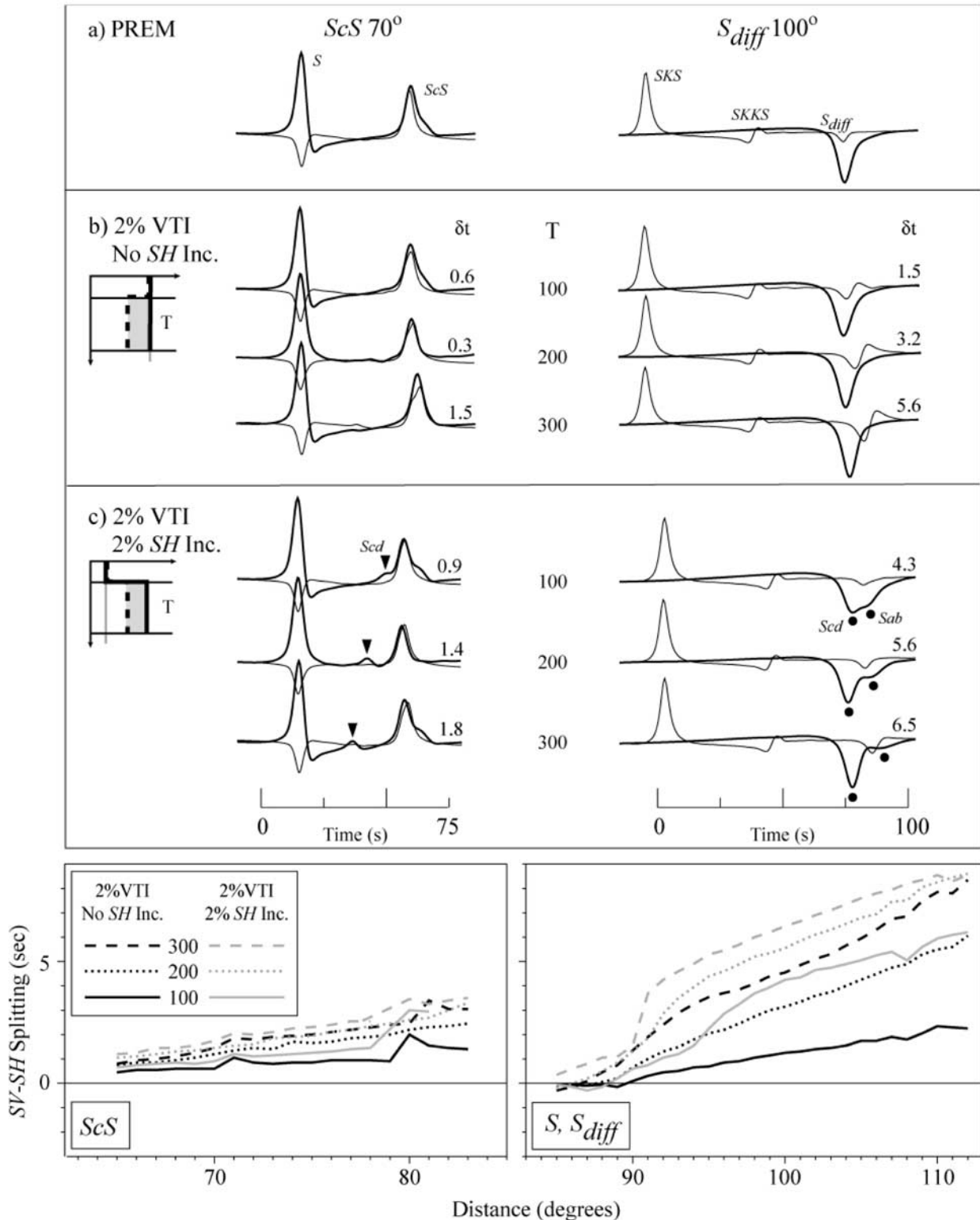
Figure 13. Synthetics at a distance of 70° and 100°. For models having different thicknesses, T, of VTI zones in D″ (indicated between the ScS and S_{diff} columns). SH seismograms are heavier lines, while SV seismograms are lighter lines. ScS traces are aligned in time and amplitude on S; S_{diff} traces are aligned in time and amplitude on SKS. Splitting times (δt) are shown to the right of each seismogram pair. (a) Synthetics for PREM. (b) Synthetics for 2% VTI with no V_{SH} discontinuity. (c) Synthetics for a 2% V_{SH} discontinuity and 2% VTI. In c), inverted triangles in the first column indicate the arrival of Scd, and solid circles (2nd column) indicate the arrival of Scd and Sab. Travel time curves are shown for Figure 13b (black lines) and Figure 13c (gray lines).
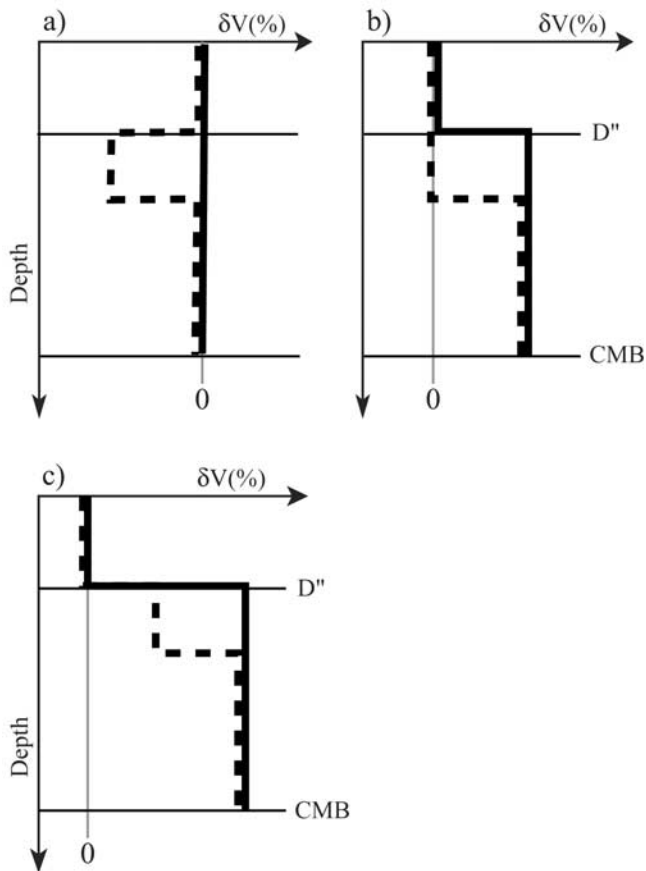
Figure 14. Schematic of models with VTI concentrated at the top of D″. V_{SH} and V_{SV} (solid and dashed lines, respectively) are shown relative to PREM (zero line). Three VTI zone thicknesses were tested: 25, 75, and 125 km. (a) Model with VTI but no V_{SH} discontinuity. (b) Model with VTI and an V_{SH} discontinuity. (c) Model with VTI and a discontinuity in V_{SH} and V_{SV}.

Splitting tends to increase with discontinuity strength and VTI zone thickness, where measurable.

[33] In principal, the strength and/or thickness of the D″ VTI zone can be increased (or decreased) to match stronger (or weaker) $SV-SH$ splitting observations. The exceptions are (1) modeling the weak splitting must have a VTI zone minimum thickness comparable to the wavelength of the observed seismic energy ($\sim$50–100 km for most past observations); (2) matching the strongest splitting with VTI magnitudes greater than a few percent can result in waveform and travel time complexities, mandating waveform comparisons between observations and synthetics; and (3) discontinuities above or below the VTI zone, as well as isotropic velocity gradients below the VTI zone, contribute to significant waveform distortions. To emphasize this point, we present synthetics for a variety of VTI structures in Figure 16. End-member model types are displayed for the S_{diff} distance range. Here our focus is the waveform shapes of the SV and SH components of S_{diff}. Different splitting magnitudes can be achieved (as previously discussed) by tuning the strength and thickness of the VTI zone.

[34] Many viable models reproduce splitting, but waveform effects can be strong and need to be considered when modeling data. To better summarize the model space, Figure 16 shows eight different VTI models. Figure 16a shows a 100 km thick VTI zone with no SH discontinuity and an anisotropy strength of 2% relative to the SH velocity. This relatively thin D″ thickness and low VTI strength results in stable S_{diff} waveforms. Splits comparable to observations are present at intermediate distances ($95°-105°$) with larger splits occurring at large epicentral distances. In contrast, Figure 16b shows the same models with a thicker (300 km) VTI zone. The first characteristic to note is the waveform complexities at short distances ($90°-95°$). As a result of VTI zone thickening larger splits become visible over the full range of distances as well as some SV complexities. Models with VTI zones placed at the top of the D″ layer were also tested. These models contained different gradients from the bottom of the VTI zone to the CMB. The third example, Figure 16c, contains an SYLO gradient [*Young and Lay*, 1990] to the CMB. This model has a VTI zone of 75 km placed at the top of a 250 km D″. A 2% SH increase and 2% anisotropy strength is given to the model. This kind of model results in very weak SV energy at larger distances and a double-peaked SV waveform at shorter distances. In Figure 16d, we increase the discontinuity strength to 4%. Complicated SV wave shape is still seen at $90°-100°$, but now we see an SV delay relative to the SH increase, which is tunable with the increase or decrease of anisotropy strength. Figure 16e exemplifies models whose gradient from the bottom of the VTI zone to the CMB takes the value of the SH velocity at that depth. Here we show a 75 km VTI zone with no SH increase and 2% anisotropy strength. The SH waveform retains it stability through the range of distances, though SV diminishes in amplitude with a broad long period onset beyond 100 degrees, making splitting difficult to measure. With the addition of a 2% SH discontinuity and 4% anisotropy (Figure 16f) larger splits result, but waveforms become more complex. At around $105°$ SV becomes too small and complex to measure. Figures 16g and 16h display models whose gradient from the bottom of the VTI zone to the CMB takes the value of the SV velocity at that depth. Figure 16g shows a 25 km VTI zone embedded at the top of a 250 km D″. The thin anisotropic zone with a 2% discontinuous SH increase and 2% anisotropy strength gives us very mild but measurable splits. After $105°$ there is not much SV energy present. By increasing the VTI thickness (Figure 16h) to 75 km, slightly larger splits are present, but no significant SV energy remains beyond $105°$.

3. Discussion

[35] In this study, shear wave splitting and waveform complexity were investigated for deep mantle lamellae and VTI models. Each model class can match data attributes. Significant waveform effects are present, however, for many models. We focus on ScS and S_{diff} splitting; S_{diff} has the longest D″ travel path and correspondingly shows the strongest waveform variability, especially for SV_{diff}. Future modeling efforts should incorporate waveform modeling of both ScS and S_{diff}.

[36] Our investigation of 1-D alternating high and low-velocity layering focused on end-members of (1) evenly spaced low-velocity lamellae in D″, and (2) approximating VTI with alternating velocities from the *Backus* [1962]
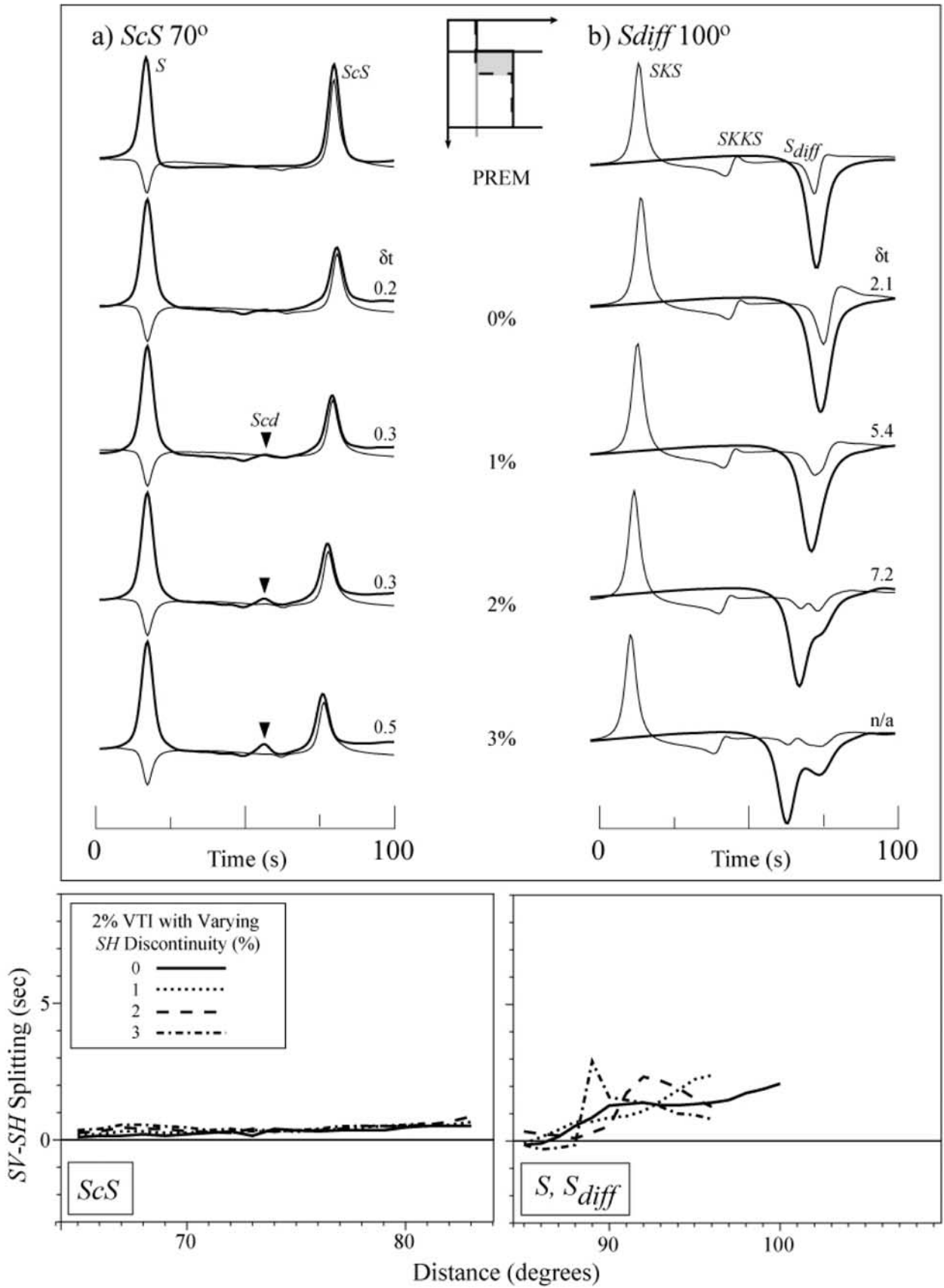
Figure 15.

formulae. Here we note that both end-members are capable of producing shear wave splitting from thin layers with strongly contrasting properties.

[37] The strength of deep mantle anisotropy is commonly estimated by distributing an observed shear wave splitting time measurement along a ray path length predicted in an assumed D″ thickness in a reference model using 1-D ray tracing. This approach can give rise to significant error due to limitations of the ray approximation [e.g., see *Garnero and Lay*, 1998]. Waveform modeling is necessary for reliable quantification of anisotropy. However, constraining the depth extent and strength of anisotropy in the deep mantle remains challenging. The origin of D″ anisotropy remains highly uncertain. Models containing either LPO [*Stixrude*, 1998; *Karato*, 1998a, 1998b; *McNamara et al.*, 2001, 2002; *Yamazaki and Karato*, 2002] or SPO [*Kendall and Silver*, 1996, 1998; *Russell et al.*, 1998, 1999] have been advanced. The development of LPO is dependent on deformation style. Experimental studies show that diffusion or superplastic creep, mainly involving grain-boundary sliding, gives rise to isotropic structures [*Karato and Li*, 1992; *Karato et al.*, 1995; *Stixrude*, 1998; *Karato*, 1998a, 1998b; *McNamara et al.*, 2001; 2002]. Thus diffusion creep is thought to dominate in isotropic portions of the lower mantle [*Karato et al.*, 1995; *McNamara et al.*, 2002]. Alternatively, LPO can develop by dislocation motion or twinning if the pressure and stress conditions are appropriate and there is strong mineralogical anisotropy [*Karato and Li*, 1992; *Stixrude*, 1998; *Karato*, 1998a, 1998b; *McNamara et al.*, 2001, 2002]. This style of deformation involves slip on an explicit glide plane, causing the crystal axes to orient in an array creating an anisotropic fabric. The dominant deformation mechanism depends on grain size, temperature, pressure, and stress or strain. Fine-grained material is susceptible to homogeneous deformation (superplasticity), while coarse grains generate strong LPO through heterogeneous deformation [*Edington et al.*, 1976; *Karato et al.*, 1995]. As stress and/or pressure increase, deformation moves into the dislocation regime, creating anisotropic regions [*Karato and Li*, 1992]. Alternatively, the simple effect of increased temperature within the superadiabatic thermal boundary layer of D″ could alone be sufficient to shift the deformation regime of the lowermost mantle into an anisotropy-inducing deformational regime, without invoking changes in poorly characterized properties such as stress or strain rates [*Lay et al.*, 1998a, 1998b]. Initial consideration of these factors, given the available predictions of elastic coefficients for primary lower mantle components, (e.g., (Mg,Fe)SiO₃ perovskite and (Mg,Fe)O magnesiowüstite which are both anisotropic) suggested difficulty in inducing LPO that corresponds to VTI with $V_{SH} > V_{SV}$ [e.g., *Stixrude*, 1998; *Kendall and Silver*, 1998].

[38] *McNamara et al.* [2001, 2002] utilize rheological parameters based on mineral physics observations [*Yamazaki and Karato*, 2001] to infer that diffusion creep dominates throughout most of the lower mantle while the deep mantle near and beneath subduction and downwellings deforms by dislocation creep. Recent work by *Yamazaki and Karato* [2002] suggests that at high pressure and in the presence of strong horizontal shear flow the slip systems activated for (Mg,Fe)O and its strong intrinsic anisotropy actually do favor development of LPO with $V_{SH} > V_{SV}$, even though (Mg,Fe)O is expected to be a small volume fraction (less than 20%) of the lower mantle. While still poorly constrained, analogue materials suggest that perovskite might develop weaker LPO in horizontal shear flows with $V_{SV} > V_{SH}$. Other mineral components, such as the high-pressure phases of SiO₂ (if present at all) might perhaps contribute to anisotropy as well [e.g., *Kendall and Silver*, 1998]. Thus, LPO might be a viable explanation of shear wave splitting in D″ if favorable mineralogy, shear flows, stress levels, and temperature conditions are present. Further mineral physics work is needed to better constrain this possibility. Our VTI modeling addresses possible LPO distributions that give rise to splitting, but neither specifies a particular mineralogy nor even requires the generation of LPO by solid-state deformation processes. In this latter respect, it is important to note that textured orientation of crystallites is a long-recognized property of crystallizing igneous intrusions [e.g., *Irvine*, 1980].

[39] Alignment of inclusions or heterogeneities with strong velocity contrasts (SPO) might also create anisotropic regions in the lower mantle. SPO could be generated by, for example, shearing of CMB reaction products [*Knittle and Jeanloz*, 1991], shearing of partially melted material brought down by subduction [*Kendall and Silver*, 1996, 1998], or the shearing or injection of near-neutrally buoyant partial melts generated in the steep thermal gradient near the CMB [*Williams and Garnero*, 1996]. Solid-state dynamic calculations suggest that warm, low-velocity regions of D″ might not be as likely to develop LPO; SPO is thus invoked as a possible cause of anisotropy in such areas [*McNamara et al.*, 2001, 2002]. Thus regions such as that beneath the central Pacific (Figure 1) are likely to require the presence of inclusions of drastically altered elastic properties. Small melt fractions are the most likely candidates for such SPO inclusions: such inclusions can result in strong anisotropy depending on the configuration of the melt [e.g., *Kendall and Silver*, 1998], and this mechanism could operate in regions in which the bulk solid is high or low velocity. In short, partial melting (and specifically melt-associated SPO) might be able to explain the suite of

Figure 15. Synthetics for VTI models with an V_{SH} velocity discontinuity of varying strengths (indicated between the columns of synthetics). *SH* synthetics are in darker lines, *SV* synthetics are in lighter lines and traces are aligned on *S* in Figure 15a and *SKS* in Figure 15b. VTI zone with a thickness of 75 km at the top of a 250 km D″ is shown, with the *S* velocity below the VTI zone being the same as the V_{SH} velocity at the base of the VTI zone. A schematic of the model is shown (also see Figure 14). Synthetics for PREM are shown at the top of each column. Splitting time between the *SV* and *SH* arrivals (δt) is shown to the right of each pair of synthetics. As in Figure 13, inverted triangles indicate the arrival of *Scd*. (a) *ScS* synthetics at 70°. Amplitudes are normalized to *S*. (b) Synthetics at 100°. Amplitudes are normalized to *SKS*. Travel times plots show splitting time versus distance. S_{diff} travel time curves do not span the entire distance window, owing to waveform complexity precluding confident splitting measurements.
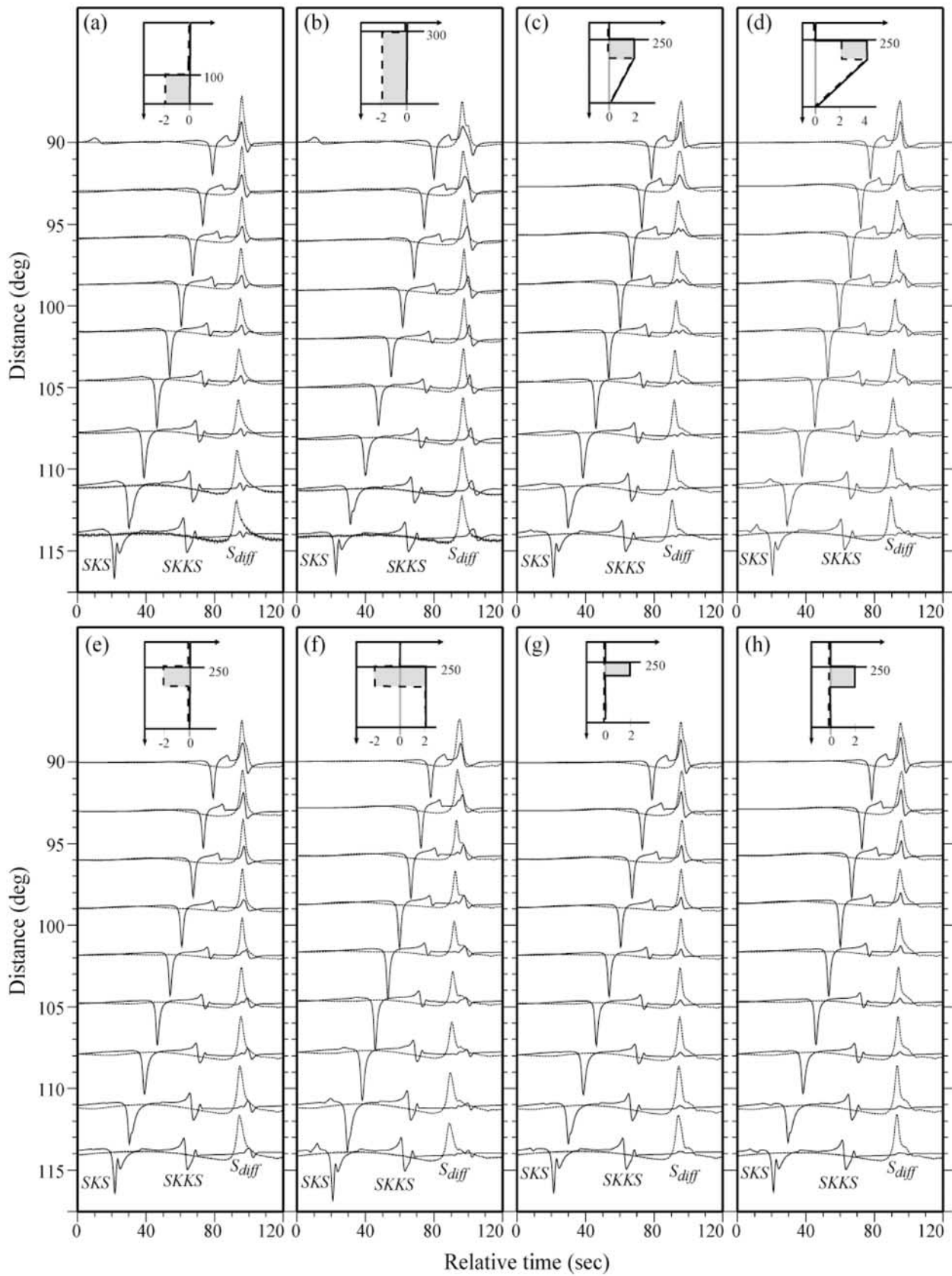
Figure 16.

seismic observations. The most likely distribution of partial melt that can explain the anisotropy is suggested by our calculations: lamellae with rapidly varying properties, whether in a moderately separated comb-like structure, or closely juxtaposed regions of variable melt content, and thus highly variable velocities, as in our VTI simulations.

[40] The key question that then arises is how melt might be entrained and distributed into sill-like features either throughout D″, or perhaps localized near the top of the zone. The factors likely to control the emplacement, stability and evolution of such partially molten zones are (1) the buoyancy of the melt; (2) the viscosity structure of D″ and the bottom portion of the overlying lower mantle; (3) the wetting behavior, and percolative velocity of melts in this region relative to advective velocities; and (4) the temperature and composition of the melt, and its degree of thermal and chemical equilibration with its neighboring solids. The unfortunate aspect of this suite of parameters is that the current state of experimental insight into melt properties at CMB conditions is minimal. A few general statements can be made, such as that silicate melts at these depths are likely to be quite inviscid, as expected from the high coordination of low-pressure "network-forming" cations such as silicon and aluminum and corresponding lack of polymerization within melts at these extreme pressures [e.g., *Williams and Jeanloz*, 1988]. In terms of the dynamics of possible melt ascent (or descent) to the top of D″, we can semi-quantitatively evaluate possible buoyancy forces on the melt. However, such buoyancy forces are not necessarily the principal factor that determines where (and whether) dikes are emplaced. Dramatic viscosity contrasts, such as those which are expected to occur due to simple thermal effects near the top of the thermal boundary layer of D″, play a critical role in magma emplacement processes [*Rubin*, 1995]. Nevertheless, whether magma segregates upward or downward plays a critical role in our inferences about the origin of melt within D″, and thus melt buoyancy does represent a parameter of interest.

[41] In order to examine how a comb-like structure of melt-rich lamellae might be formed or maintained above the CMB, we conduct calculations of solid-liquid buoyancy contrasts for CMB melts. These calculations are designed to simply explore whether regions in parameter space exist in which it is possible to generate neutrally buoyant melts within the bulk of D″. As our knowledge of melt properties is highly uncertain at CMB conditions, we simply take a plausible range of parameters and calculate how close to neutral buoyancy melts might be under these conditions. Our initial assumption is that melts are generated within D″, possibly at the top of the partially molten ULVZ: from this depth, many melts likely remain pinned by negative buoyancy near the CMB. We assume that much of D″ lies above the solidus of material of fertile CMB composition (as opposed to regions that have undergone melt extraction). Moreover, because melt ascent via either dissolution and reprecipitation or porous flow is likely, we assume that melts partially thermally equilibrate on ascent. Specifically, we assume that full thermal equilibration occurs by the top of D″. The principal effects on such buoyancy calculations are produced by (1) the effect of solid/liquid iron-partitioning; (2) the composition of solid phases that melt to produce the liquid; (3) the volume change on melting and (4) the difference in thermal expansion between the liquid and coexisting solids (assuming that the liquid has thermally equilibrated). Indeed, the trade-offs in buoyancy between the iron content of CMB liquids and their volumes of fusion has previously been explored for melts within the ULVZ [*Knittle*, 1998]: we incorporate an additional thermal expansion effect here for melts emplaced at different depths within the steep thermal gradient of D″. Solid/melt partition coefficients of iron between perovskite and melt are estimated to be 0.23 (±0.11), indicating that melts are markedly enriched in iron relative to their coexisting solids [*Knittle*, 1998]: this value has been determined at primarily shallow to middle-lower mantle pressures, and its pressure dependence is ill constrained. As the value of the partition coefficient is similar under these lower pressure conditions to that between perovskite and magnesiowüstite, we assume that the iron relevant partition coefficient near the base of the mantle has similar pressure dependence to that documented in the solid-state perovskite-magnesiowüstite system [*Mao et al.*, 1997]. Our rationale for this assumption is simply that iron appears to become more compatible within perovskite at high pressures, and we expect this chemical tendency to be reflected in the perovskite-melt partition coefficients, as well. It is likely that any eutectic between magnesiowüstite and perovskite lies closer to silicate perovskite, in accord with observations of melting of such assemblages under lower mantle conditions [e.g., *Williams*, 1990; *Ito and Katsura*, 1992]. However, the state of knowledge of melt chemistries under these conditions is such that our illustrative calculations can only qualitatively

Figure 16. Summary figure for different classes of VTI models. Seismograms are shown in distance (degrees) versus relative time in seconds. All traces are aligned in time on the S_{diff} and amplitudes are scaled to the largest amplitude in the time window. *SKS*, *SKKS*, and S_{diff} arrivals are indicated. V_{SH} is indicated by the dashed lines and V_{SV} by the solid lines. A schematic of each model is shown above each set of seismograms. (a) VTI zone throughout a 100 km D″, with no V_{SH} increase and 2% anisotropy. (b) VTI zone throughout a 300 km D″, with no V_{SH} increase and 2% anisotropy. (c) A 75 km VTI zone placed at the top of a 250 km D″ using a SYLO gradient from the bottom of the VTI zone to the CMB, with a 2% V_{SH} increase and 2% anisotropy. (d) A 75 km VTI zone placed at the top of a 250 km D″ using a SYLO gradient [*Young and Lay*, 1990] from the bottom of the VTI zone to the CMB, with a 2% V_{SH} increase and 4% anisotropy. (e) A 75 km VTI zone placed at the top of a 250 km D″ using the value of V_{SH} at the bottom of the VTI zone as a gradient down to the CMB, with no V_{SH} increase and 2% anisotropy. (f) A 75 km VTI zone placed at the top of a 250 km D″ using the value of V_{SH} at the bottom of the VTI zone as a gradient down to the CMB, with a 2% V_{SH} increase and 4% anisotropy. (g) A 25 km VTI zone placed at the top of a 250 km D″ using the value of V_{SV} at the bottom of the VTI zone as a gradient down to the CMB, with a 2% V_{SH} increase and 2% anisotropy. (h) A 75 km VTI zone placed at the top of a 250 km D″ using the value of V_{SV} at the bottom of the VTI zone as a gradient down to the CMB, with a 2% V_{SH} increase and 2% anisotropy. See text for details.
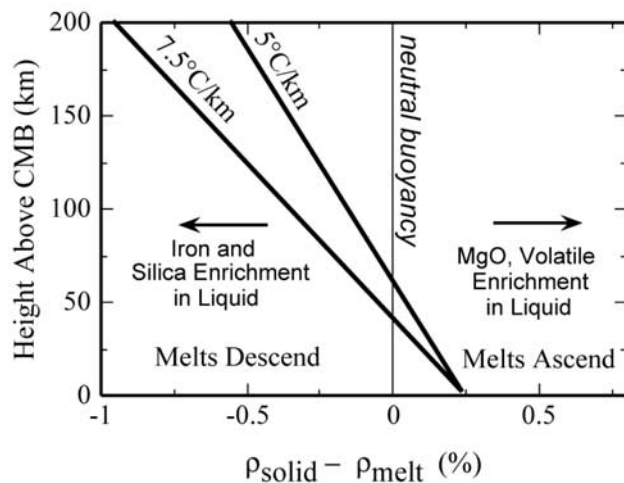
Figure 17. Illustrative calculation of possible relative melt-solid density contrasts within D″ given as height above CMB in kilometers versus % density change from solid to melt. Melt density contrasts for two different thermal gradients are shown, with a clear density cross-over occurring between 40 and 100 km above the CMB. Clearly, small changes in chemistry or temperature could generate melts that would be concentrated at either the bottom of D″, if weakly negatively buoyant, or the nearest upward rheological discontinuity. Horizontal arrows indicate the effects that increasing concentrations of different chemical components within the melts are likely to have on the calculated density contrasts.

indicate the effect of melt chemistry on its buoyancy. Thermal effects on the melts are calculated by assuming that the thermal expansion of the melts exceeds that of the coexisting solids by 8×10^{-6}/K. This value is highly uncertain, as no constraints exist on the thermal expansion of melts at these conditions, and even the thermal expansion of solids under CMB conditions is controversial. We choose this value simply because phases such as MgO are inferred to have a thermal expansion of $10-16 \times 10^{-6}$ at 2000 K and CMB pressures [*Duffy and Ahrens*, 1993]. At the more likely temperatures (near 4000 K) of the CMB, higher thermal expansions are expected, and non-network forming melts in turn typically have higher thermal expansions than their associated solids [e.g., *Lange and Carmichael*, 1990]. We utilize this thermal expansion in tandem with constant temperature gradients across the lowermost 200 km of the mantle, corresponding to gradients within the thermal boundary layer of 5°/km and 7.5°/km [e.g., *Williams*, 1998]. Finally, we approximate the volume of fusion as +1.0%, which is in accord with volumes derived from studies of shocked liquids and materials melting under shock-loading at lower mantle conditions [*Brown et al.*, 1987; *Rigden et al.*, 1989].

[42] Figure 17 shows the likely critical dependence of buoyancy on the chemistry and temperature of emplaced melt at CMB conditions: depths of neutral buoyancy are encountered for our model melts between 40 and 80 km above the CMB. Obviously, if the melt is more iron-enriched, it will be negatively buoyant and likely pinned near the CMB; if more enriched in MgO, or in volatiles (such as water or carbon), melts will be neutrally buoyant at shallower depths. It has long been appreciated that melts and solids likely approach one another in density near CMB pressures [*Rigden et al.*, 1989; *Williams and Garnero*, 1996; *Knittle*, 1998; *Ohtani and Maeda*, 2001]. The primary point here is that chemical and thermal effects might be able to produce suites of melts that are neutrally buoyant at depths spanning those within D″.

[43] Such melt emplacement within D″ is ideal for generating the anisotropic comb-like structures shown in Figure 4 above (though we note our 1-D modeling precludes testing of vertically oriented structures). The physical origin for this neutral buoyancy lies in a combination of the effect of iron partitioning in densifying the melt, and allowing the melt to thermally contract on ascent, thus reducing its buoyancy as it moves through D″: the combination of these two effects counterbalances the effect of the increase in volume on fusion. Thus, a range of depths of melt neutral buoyancy could be accessed depending on the degree of thermal equilibration of the melt. Notably, shifts in the chemistry of the melt through precipitation of solids is likely under such conditions: given that these solids will likely be iron-depleted, the cooling and (partial) solidification process could result in melt densification and possible gradual descent over time. Nevertheless, the style and magnitude of double-diffusive processes that might occur within a partially molten D″ are completely speculative: however, we are encouraged in our lamellae-based modeling by the observations of cyclic units in solidified igneous intrusions. Such cyclic units involve repetitive sequences of precipitated minerals, often on the ∼100 m length scale, that have been associated with repeated injections of magma from beneath [e.g., *Irvine*, 1980]. During the solidification of such features, horizontal lamellae of melt presumably existed at different stratigraphic heights within the intrusion: a close analog to the comb-like partially molten structures we propose might exist within D″.

[44] Buoyancy calculations such as those of Figure 17 are primarily relevant to the initial emplacement of melt-rich lamellae: over time, these lamellae will likely chemically evolve through precipitation of solid phases, and eventually thermally equilibrate with their surrounding solids. The processes by which such melts chemically evolve are likely to be complex. For example, although laboratory observations of melts at even middle-lower mantle conditions are sparse, robust Soret diffusion has been documented in silicate melts at such conditions [*Heinz and Jeanloz*, 1987]. Such temperature-gradient driven chemical diffusion might be anticipated to be important from the broad viewpoint of magma emplacement and transport occurring within a zone that has possibly the largest superadiabatic temperature change within the planet. For systems in which the Soret potential is larger than the gradient in liquid composition along the limb of the eutectic, the melt will chemically evolve toward a lower-temperature melt composition nearer the eutectic, with higher temperature residual solids forming as cumulates [*Lesher and Walker*, 1988]. Therefore, if melts with temperatures greater than their eutectic rise, or are entrained in upwellings from the ULVZ, it is possible that they could chemically evolve to form lower-temperature melts, as they thermally equilibrate with
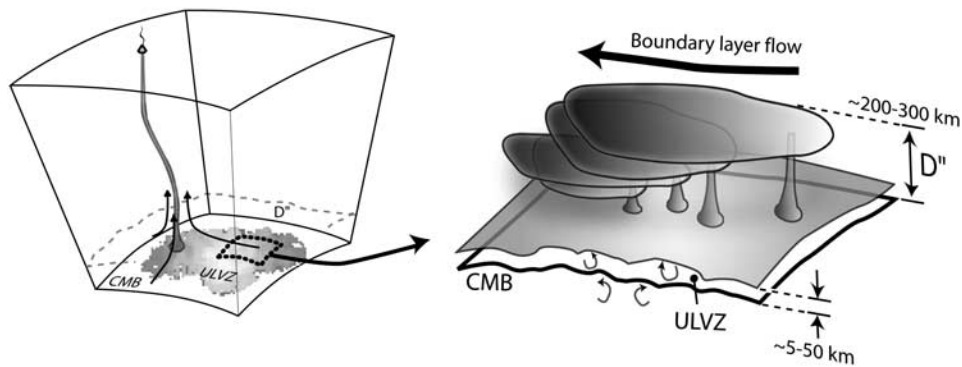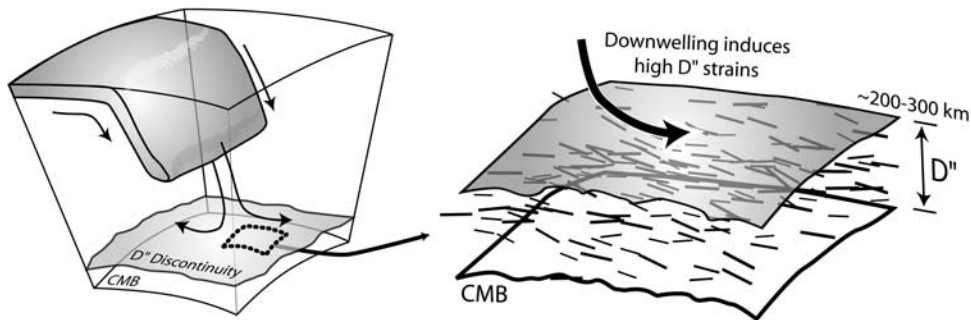
Figure 18. Two possible D″ scenarios that correspond to lamellae and VTI model types. (a) SPO near an upwelling. There may be melt present in D″ that spans a range of chemistries (from weakly positive to weakly negatively buoyant). These melts can be concentrated at either the bottom, if weakly negatively buoyant, or at the nearest upward rheological contrast (since melts tend to pond at rheologic discontinuities), e.g., at the top of D″. It might be possible to distribute relative flat lying melt through pervasive diking along with shearing boundary flow at the top of the TBL forming thin layers of contrasting properties as explored with the lamellae models. (b) LPO beneath a slab. Downwellings might induce high strains that might align crystals into a preferred orientation creating VTI conducive to shear wave splitting as explored in the VTI models.

their surrounding solids. The key point here is that there are effects that can generate suites of melts of different chemistry, and thus differing depths of neutral buoyancy: precisely the type of physical process that might produce dikes or sills at differing depths within D″.

[45] Although dikes and sills are essentially ubiquitous in magmatic systems near the Earth's surface, the geometry of igneous intrusions within D″ is speculative. However, the concept that melt-rich channels could persist within the viscous mantle is certainly not new [e.g., *Arzi*, 1978]. What is clear is that if partially molten zones exist in the basal layer, melt from this zone might rise, or be entrained, to shallower depths. The comb-like models pursued here are implicitly sills of nominally infinite lateral extent. We view these as a simple end-member: we obviously do not have a constraint on the aspect ratios of partial melt-rich regions within D″, and do not preclude that ubiquitous horizontal diking, rather than sill formation (among other possible scenarios, as discussed earlier), could be present. In this context, we simply note that the most critical parameter in determining the magnitude of shear-wave splitting was the amount of partially molten material suspended within D″. As long as the emplaced partially molten features are

approximately horizontal, we would expect that similar abundances of partially molten material would yield similar splitting. In passing, we note that horizontally emplaced partially molten features could be particularly long-lived: vertically angled features might be transient, with drainage occurring either upward or downward. Moreover, if the uppermost boundary of D″ represents either a chemical discontinuity, or is simply a viscosity contrast due to the lower temperatures within the overlying lower mantle relative to those in D″, the top of D″ could be a plausible region in which melts could pool and be distributed laterally through diking or sill formation. This manner of emplacement provides a natural mechanism for concentrating partial-melt filled lamellae near the top of D″, thus giving rise to the most effective comb-geometry for generating the observed shear-wave splitting (Figure 8).

[46] Figure 18 schematically illustrates two possibilities for the evolution of anisotropic textures in D″. Boundary layer shear flow that that feeds plumes and upwellings can shear either products of chemical reactions between the silicate mantle and iron-alloy outer core [e.g., *Knittle and Jeanloz*, 1989], or ascending melt rich instabilities from an ultra-low-velocity zone layer (Figure 17a). Indeed, the

partially molten regions themselves could provide zones permitting locally high shear strain, thus providing a locale for flow localization and corresponding lateral expansion through shear of the partially molten zone. In turn, viscous heating could preserve and/or augment the amount of partial melt in these sills. Beneath downwellings, the high strains might give rise to D″ LPO (Figure 18b).

[47] A major challenge for seismology is to better constrain the geometry and mechanism of seismic anisotropy in the deep mantle. This will involve more completely accounting for effects of upper mantle anisotropy as well as conducting seismic experiments that offer a greater range of azimuthal sampling of D″ regions. At present, all regional studies of deep mantle anisotropy suffer from very limited azimuthal coverage, leaving uncertainty in the symmetry orientations of anisotropic material. Modeling efforts should also incorporate waveform information to reduce solution model uncertainties that arise for splitting time analyses.

4. Conclusions

[48] Modeling D″ structure with low-velocity lamellae models indicates that a modest number of partial melt layers sheared out in the boundary layer can produce grazing S wave splitting magnitudes and range dependence that match observations. For a model space of 1-D structures, these melt layers must comprise >3% and no more than 15–20% of D″ by volume, depending on the velocity perturbation properties, to develop significant splits that fall within the range of observed splitting. More steeply incident ScS phases are typically not significantly split by such models, though their travel times can be affected.

[49] Using periodic structures that achieve long wavelength vertical transverse isotropy can match both ScS and S_{diff} observed splitting magnitudes, along with complexities such as variable appearance of triplications in SV and SH waveforms. Relatively thin zones (<75 km thick) of anisotropic material within D″ might exist with 2–3% VTI and produce splitting. A thicker layer might be present but must have weaker anisotropy or splits become too large to match observations, e.g., a 300 km zone with 2% VTI gives relatively large splitting measurements of 5.6 s or greater depending on the epicentral distance (e.g., see Figure 13). Very detailed waveform analysis appears to be the most promising approach to better constraining the depth extent of anisotropy. Large isotropic velocity perturbations in the alternating layers are required to achieve the desired VTI, so it seems likely that this case approximates anisotropy induced by LPO of suitable lower mantle minerals ((Mg,Fe)O appears to be one viable candidate), or SPO of small scale inclusions such as horizontally distributed disks of partial melt. Future studies incorporating simultaneous analysis of P and S wave behavior might help to separate thermal and chemical contributions from the anisotropic properties. Certainly, simultaneous analysis of anisotropy, heterogeneity and D″ discontinuity structure might be necessary to constrain an overall model of the boundary layer [Garnero and Lay, 2003].

References

Arzi, A. A. (1978), Critical phenomena in the rheology of partially melted rocks, *Tectonophysics*, *44*, 173–184.

Backus, G. E. (1962), Long-wave elastic anisotropy produced by horizontal layering, *J. Geophys. Res.*, *67*, 4427–4440.

Bolton, H., and G. Masters (2001), Travel times of P and S from the global digital seismic networks: Implications for the relative variation of P and S velocity in the mantle, *J. Geophys. Res.*, *106*, 13,527–13,540.

Brown, J. M., M. D. Furnish, and R. G. McQueen (1987), Thermodynamics for (Mg,Fe)₂SiO₄ from the Hugoniot, in *High Pressure Research in Mineral Physics*, *Geophys. Monogr. Ser.*, vol. 39, edited by M. H. Manghnani and Y. Syono, pp. 373–384, AGU, Washington, D. C.

Cormier, V. F. (1999), Anisotropy of heterogeneity scale lengths in the lower mantle from PKIKP precursors, *Geophys. J. Int.*, *136*, 373–384.

Cormier, V. F. (2000), D″ as a transition in the heterogeneity spectrum of the lowermost mantle, *J. Geophys. Res.*, *105*, 16,193–16,205.

Ding, X., and D. V. Helmberger (1997), Modeling D″ structure beneath Central America with broadband seismic data, *Phys. Earth Planet. Inter.*, *101*, 245–270.

Duffy, T. S., and T. J. Ahrens (1993), Thermal expansion of mantle and core materials at very high pressure, *Geophys. Res. Lett.*, *20*, 1103–1106.

Dziewonski, A. M., and D. L. Anderson (1981), Preliminary reference Earth model, *Phys. Earth Planet. Inter.*, *25*, 297–356.

Edington, J. W., K. N. Melton, and C. P. Cutler (1976), Superplasticity, *Prog. Mater. Sci.*, *21*, 63–170.

Fouch, M. J., K. M. Fischer, and M. E. Wysession (2001), Lowermost mantle anisotropy beneath the Pacific: Imaging the source of the Hawaiian plume, *Earth Planet. Sci. Lett.*, *190*, 167–180.

Fuchs, K., and G. Müller (1971), Computation of synthetic seismograms with the reflectivity method and comparison with observations, *Geophys. J. R. Astron. Soc.*, *23*, 417–433.

Garnero, E. J. (2000), Heterogeneity of the lowermost mantle, *Annu. Rev. Earth Planet. Sci.*, *28*, 509–537.

Garnero, E. J., and T. Lay (1997), Lateral variations in lowermost mantle shear wave anisotropy beneath the north Pacific and Alaska, *J. Geophys. Res.*, *102*, 8121–8135.

Garnero, E. J., and T. Lay (1998), Effects of D″ anisotropy on seismic velocity models of the outermost core, *Geophys. Res. Lett.*, *25*, 2341–2344.

Garnero, E. J., and T. Lay (2003), D″ shear velocity heterogeneity, anisotropy, and discontinuity structure beneath the Caribbean and Central America, *Phys. Earth Planet. Inter.*, *140*, 219–242.

Garnero, E. J., J. S. Revenaugh, Q. Williams, T. Lay, and L. H. Kellogg (1998), Ultralow-velocity zone at the core-mantle boundary, in *The Core-Mantle Boundary Region*, *Geodyn. Ser.*, vol. 28, edited by M. Gurnis et al., pp. 319–334, AGU, Washington, D. C.

Gurnis, M., M. E. Wysession, E. Knittle, and B. A. Buffett (Eds.) (1998), *The Core-Mantle Boundary Region*, *Geodyn. Ser.*, 28, 334 pp., AGU, Washington, D. C.

Heinz, D. L., and R. Jeanloz (1987), Measurement of the melting curve of (Mg,Fe)SiO₃ at lower mantle conditions and its geophysical implications, *J. Geophys. Res.*, *92*, 11,437–11,444.

Holland, K. G., and T. J. Ahrens (1997), Melting of (Mg,Fe)₂SiO₄ at the core-mantle boundary of the Earth, *Science*, *275*, 1623–1625.

Irvine, T. N. (1980), Magmatic infiltration metasomatism, double-diffusive fractional crystallization, and adcumulus growth in the Muskox and other layered intrusions, in *Physics of Magmatic Processes*, edited by R. B. Hargraves, pp. 325–383, Princeton Univ. Press, Princeton, N. J.

Ito, E., and T. Katsura (1992), High pressure melting of ferromagnesian silicates under the lower mantle conditions, in *High Pressure Research: Application to Earth and Planetary Sciences*, *Geophys. Monogr. Ser.*, vol. 67, edited by Y. Syono and M. H. Manghnani, pp. 315–322, AGU, Washington, D. C.

Kaneshima, S., and P. G. Silver (1995), Anisotropic loci in the mantle beneath central Peru, *Phys. Earth Planet. Inter.*, *88*, 257–272.

Karato, S. (1998a), Some remarks on the origin of seismic anisotropy in the D″ layer, *Earth Planets Space*, *50*, 1019–1028.

Karato, S. I. (1998b), Seismic anisotropy in the deep mantle, boundary layers and the geometry of mantle convection, *Pure Appl. Geophys.*, *151*, 565–587.

Karato, S., and P. Li (1992), Diffusion creep in perovskite: Implications for the rheology of the lower mantle, *Science*, *255*, 1238–1240.

Karato, S., S. Q. Zhang, and H. R. Wenk (1995), Superplasticity in Earth's lower mantle: Evidence from seismic anisotropy and rock physics, *Science*, *270*, 458–461.

Kendall, J. M. (2000), Seismic anisotropy in the boundary layers of the mantle, in *Earth's Deep Interior: Mineral Physics and Tomography From the Atomic to the Global Scale*, *Geophys. Monogr. Ser.*, vol. 117, edited by S. Karato et al., pp. 133–159, AGU, Washington, D. C.

Kendall, J. M., and P. G. Silver (1996), Constraints from seismic anisotropy on the nature of the lowermost mantle, *Nature*, *381*, 409–412.

Kendall, J. M., and P. G. Silver (1998), Investigating causes of D″ anisotropy, in *The Core-Mantle Boundary Region*, *Geodyn. Ser.*, vol. 28, edited by M. Gurnis et al., pp. 97–118, AGU, Washington, D. C.

Kennett, B. L. N., S. Widiyantoro, and R. D. van der Hilst (1998), Joint seismic tomography for bulk sound and shear wave speed in the Earth's mantle, *J. Geophys. Res.*, *103*, 12,469–12,493.

Kind, R., and G. Müller (1975), Computations of SV waves in realistic earth models, *J. Geophys.*, *41*, 149–175.

Knittle, E. (1998), The solid/liquid partitioning of major and radiogenic elements at lower mantle pressures: Implications for the core-mantle boundary region, in *The Core-Mantle Boundary Region*, *Geodyn. Ser.*, vol. 28, edited by M. Gurnis et al., pp. 119–130, AGU, Washington, D. C.

Knittle, E., and R. Jeanloz (1989), Simulating the core-mantle boundary: An experimental study of high-pressure reactions between silicates and liquid iron, *Geophys. Res. Lett.*, *16*, 609–612.

Knittle, E., and R. Jeanloz (1991), Earth's core-mantle boundary: Results of experiments at high pressures and temperatures, *Science*, *251*, 1438–1443.

Lange, R. L., and I. S. E. Carmichael (1990), Thermodynamic properties of silicate liquids with emphasis on density, thermal expansion and compressibility, *Rev. Mineral.*, *24*, 25–64.

Lay, T., and D. V. Helmberger (1983), The shear-wave velocity-gradient at the base of the mantle, *J. Geophys. Res.*, *88*, 8160–8170.

Lay, T., and C. J. Young (1990), The stably stratified outermost core revisited, *Geophys. Res. Lett.*, *17*, 2001–2004.

Lay, T., and C. J. Young (1991), Analysis of seismic SV waves in the core's penumbra, *Geophys. Res. Lett.*, *18*, 1373–1376.

Lay, T., Q. Williams, and E. J. Garnero (1998a), The core-mantle boundary layer and deep Earth dynamics, *Nature*, *392*, 461–468.

Lay, T., Q. Williams, E. J. Garnero, L. Kellogg, and M. E. Wysession (1998b), Seismic wave anisotropy in the D″ region and its implications, in *The Core-Mantle Boundary Region*, *Geodyn. Ser.*, vol. 28, edited by M. Gurnis et al., pp. 299–318, AGU, Washington, D. C.

Lesher, C. E., and D. Walker (1988), Cumulate maturation and melt migration in a temperature gradient, *J. Geophys. Res.*, *93*, 10,295–10,311.

Loper, D. E., and T. Lay (1995), The core-mantle boundary region, *J. Geophys. Res.*, *100*, 6397–6420.

Mao, H. K., G. Shen, and R. J. Hemley (1997), Multivariable dependence of Fe-Mg partitioning in the lower mantle, *Science*, *278*, 2098–2100.

Masters, G., G. Laske, H. Bolton, and A. Dziewonski (2000), The relative behavior of shear velocity, bulk sound speed, and compressional velocity in the mantle: Implications for chemical and thermal structure, in *Earth's Deep Interior: Mineral Physics and Tomography From the Atomic to the Global Scale*, *Geophys. Monogr. Ser.*, vol. 117, edited by S. Karato et al., pp. 63–87, AGU, Washington, D. C.

Matzel, E., M. K. Sen, and S. P. Grand (1996), Evidence for anisotropy in the deep mantle beneath Alaska, *Geophys. Res., Lett.*, *23*, 2417–2420.

Maupin, V. (1994), On the possibility of anisotropy in the D″ layer as inferred from the polarization of diffracted S-waves, *Phys. Earth Planet. Inter.*, *87*, 1–32.

McNamara, A. K., S. Karato, and P. E. van Keken (2001), Localization of dislocation creep in the lower mantle: Implications for the origin of seismic anisotropy, *Earth Planet. Sci. Lett.*, *191*, 85–99.

McNamara, A. K., P. E. van Keken, and S. I. Karato (2002), Development of anisotropic structure in the Earth's lower mantle by solid-state convection, *Nature*, *416*, 310–314.

Meade, C., P. G. Silver, and S. Kaneshima (1995), Laboratory and seismological observations of lower mantle isotropy, *Geophys. Res. Lett.*, *22*, 1293–1296.

Mitchell, B. J., and D. V. Helmberger (1973), Shear velocities at base of mantle from observations of S and ScS, *J. Geophys. Res.*, *78*, 6009–6020.

Moore, M. M., E. J. Garnero, and T. Lay (2002), D″ anisotropy beneath the Atlantic Ocean and the southern Pacific Ocean, *Eos. Trans. AGU*, *83*(47), Fall. Meet. Suppl., Abstract S12D-10.

Müller, G. (1985), The reflectivity method: A tutorial, *J. Geophys.*, *58*, 153–174.

Ni, S., E. Tan, M. Gurnis, and D. Helmberger (2002), Sharp sides to the African superplume, *Science*, *296*, 1850–1852.

Ohtani, E., and M. Maeda (2001), Density of basaltic melt at high pressure and stability of the melt at the base of the mantle, *Earth Planet. Sci. Lett.*, *193*, 69–75.

Pulliam, J., and M. K. Sen (1998), Seismic anisotropy in the core-mantle transition zone, *Geophys. J. Int.*, *135*, 113–128.

Rigden, S. M., T. J. Ahrens, and E. M. Stolper (1989), High-pressure equation of state of molten anorthite and diopside, *J. Geophys. Res.*, *94*, 9508–9522.

Ritsema, J. (2000), Evidence for shear velocity anisotropy in the lowermost mantle beneath the Indian Ocean, *Geophys. Res. Lett.*, *27*, 1041–1044.

Ritsema, J., E. Garnero, and T. Lay (1997), A strongly negative shear velocity gradient and lateral variability in the lowermost mantle beneath the Pacific, *J. Geophys. Res.*, *102*, 20,395–20,411.

Ritsema, J., T. Lay, E. J. Garnero, and H. Benz (1998), Seismic anisotropy in the lowermost mantle beneath the Pacific, *Geophys. Res. Lett.*, *25*, 1229–1232.

Robertson, G. S., and J. H. Woodhouse (1996), Ratio of relative S to P velocity heterogeneity in the lower mantle, *J. Geophys. Res.*, *101*, 20,041–20,052.

Rubin, A. M. (1995), Propagation of magma-filled cracks, *Annu. Rev. Earth Planet. Sci.*, *23*, 287–336.

Russell, S. A., T. Lay, and E. J. Garnero (1998), Seismic evidence for small-scale dynamics in the lowermost mantle at the root of the Hawaiian hotspot, *Nature*, *396*, 255–258.

Russell, S. A., T. Lay, and E. J. Garnero (1999), Small-scale lateral shear velocity and anisotropy heterogeneity near the core-mantle boundary beneath the central Pacific imaged using broadband ScS waves, *J. Geophys. Res.*, *104*, 13,183–13,199.

Russell, S. A., C. Reasoner, T. Lay, and J. Revenaugh (2001), Coexisting shear- and compressional-wave seismic velocity discontinuities beneath the central Pacific, *Geophys. Res. Lett.*, *28*, 2281–2284.

Saltzer, R. L., R. D. van der Hilst, and H. Karason (2001), Comparing P and S wave heterogeneity in the mantle, *Geophys. Res. Lett.*, *28*, 1335–1338.

Simmons, N. A., and S. P. Grand (2002), Partial melting in the deepest mantle, *Geophys. Res. Lett.*, *29*(11), 1552, doi:10.1029/2001GL013716.

Steinbach, V., and D. A. Yuen (1999), Viscous heating: A potential mechanism for the formation of the ultralow-velocity zone, *Earth Planet. Sci. Lett.*, *172*, 213–220.

Stixrude, L. (1998), Elastic constants and anisotropy of $MgSiO_3$ perovskite, periclase, and SiO_2 at high pressure, in *The Core-Mantle Boundary Region*, *Geodyn. Ser.*, vol. 28, edited by M. Gurnis et al., pp. 83–96, AGU, Washington, D. C.

Su, W. J., and A. M. Dziewonski (1997), Simultaneous inversion for 3-D variations in shear and bulk velocity in the mantle, *Phys. Earth Planet. Inter.*, *100*, 135–156.

Thomas, C., and J.-M. Kendall (2002), The lowermost mantle beneath northern Asia: (2) Evidence for D″ anisotropy, *Geophys. J. Int.*, *151*, 296–308.

Thomas, C., M. Weber, A. Agnon, and A. Hofstetter (1998), A low-velocity lamella in D″, *Geophys. Res. Lett.*, *25*, 2885–2888.

Vinnik, L., F. Farra, and B. Romanowicz (1989), Observational evidence for diffracted SV in the shadow of the Earth's core, *Geophys. Res. Lett.*, *16*, 519–522.

Vinnik, L., B. Romanowicz, Y. Lestunff, and L. Makeyeva (1995), Seismic anisotropy in the D″ layer, *Geophys. Res. Lett.*, *22*, 1657–1660.

Vinnik, L., L. Breger, and B. Romanowicz (1998), Anisotropic structures at the base of the Earth's mantle, *Nature*, *393*, 564–567.

Weber, M. (1994), Lamellae in D″?: An alternative model for lower mantle anomalies, *Geophys. Res. Lett.*, *21*, 2531–2534.

Wen, L. (2002), An SH hybrid method and shear velocity structures in the lowermost mantle beneath the central Pacific and South Atlantic Oceans, *J. Geophys. Res.*, *107*(B3), 2055, doi:10.1029/2001JB000499.

Wen, L. X., and D. V. Helmberger (1998), Ultra-low-velocity zones near the core-mantle boundary from broadband PKP precursors, *Science*, *279*, 1701–1703.

Wen, L., P. Silver, D. James, and R. Kuehnel (2001), Seismic evidence for a thermo-chemical boundary at the base of the Earth's mantle, *Earth Planet. Sci. Lett.*, *189*, 141–153.

Williams, Q. (1990), Molten ($Mg_{0.88}$, $Fe_{0.12}$)$_2SiO_4$ at lower mantle conditions: Melting products and structure of quenched glasses, *Geophys. Res. Lett.*, *17*, 635–638.

Williams, Q. (1998), The temperature contrast across D″, in *The Core-Mantle Boundary Region*, *Geodyn. Ser.*, vol. 28, edited by M. Gurnis et al., pp. 73–81, AGU, Washington, D. C.

Williams, Q., and E. J. Garnero (1996), Seismic evidence for partial melt at the base of Earth's mantle, *Science*, *273*, 1528–1530.

Williams, Q., and R. Jeanloz (1988), Spectroscopic evidence for pressure-induced coordination changes in silicate glasses and melts, *Science*, *239*, 902–905.

Wookey, J., J.-M. Kendall, and G. Barruol (2002), Mid-mantle deformation inferred from seismic anisotropy, *Nature*, *415*, 777–780.

Wysession, M. E., T. Lay, J. Revenaugh, Q. Williams, E. J. Garnero, R. Jeanloz, and L. Kellogg (1998), The D″ discontinuity and its implications, in *The Core-Mantle Boundary Region*, *Geodyn. Ser.*, vol. 28, edited by M. Gurnis et al., pp. 273–298, AGU, Washington, D. C.

Wysession, M. E., A. Langenhorst, M. J. Fouch, K. M. Fischer, G. I. Al-Eqabi, P. J. Shore, and T. J. Clarke (1999), Lateral variations in compressional/shear velocities at the base of the mantle, *Science*, *284*, 120–125.

Yamazaki, D., and S. Karato (2001), Some mineral physics constraints on the rheology and geothermal structure of Earth's lower mantle, *Am. Mineral.*, *86*, 385–391.

Yamazaki, D., and S. Karato (2002), Fabric development in (Mg, Fe)O during large strain, shear deformation: Implications for seismic anisot-ropy in Earth's lower mantle, *Phys. Earth Planet. Inter.*, *251*, 251–267.

Young, C. J., and T. Lay (1990), Multiple phase analysis of the shear velocity structure in the D″ region beneath Alaska, *J. Geophys. Res.*, *95*, 17,385–17,402.

Zerr, A., A. Diegeler, and R. Boehler (1998), Solidus of the Earth's deep mantle, *Science*, *281*, 243–245.

_____

E. J. Garnero and M. M. Moore, Department of Geological Sciences, Arizona State University, Box 871404, Tempe, AZ 85287-1404, USA. (melissa.m.moore@asu.org)

T. Lay and Q. Williams, Earth Sciences Department, University of California, Santa Cruz, 1156 High Street, Santa Cruz, CA 95064, USA.